Burchill and Knudsen
Earth, Planets and Space (2022) 74:181
https://doi.org/10.1186/s40623-022-01736-w

Earth, Planets and Space

FULL PAPER

Open Access

Swarm Thermal Ion Imager measurement performance

Johnathan K. Burchill[1*] and David J. Knudsen[1]

Abstract

We assess the performance of the thermal ion imaging (TII) technique as conceived for the Swarm Earth Explorer satellites. Analysis, simulation, and laboratory testing performed prior to flight provided estimates of systematic and random error sources of the electric field instrument's vector ion drift, electric field, and ion kinetic temperature measurements. An end-to-end instrument simulator, consisting of models of the TIIs on a prototypical Swarm satellite orbiting Earth with ionospheric plasma, electric field, and magnetic field inputs, was used to generate TII sensor data (level 0 instrument data). These data were processed with a prototype processor (the level 1b processor) to characterize theoretical measurement performance. We describe the methodology used to assess TII measurement uncertainty and present the main findings of the end-to-end measurement performance study. In addition, we assess the measurement performance achieved during approximately eight years of orbital operations. Example measurements demonstrate the quality of ion drift velocity. Unprocessed TII imagery reveals spurious signals which can affect measurement performance. Availability of such imagery has proven vital for diagnosing measurement anomalies associated with sensor operation and spacecraft–plasma interactions.

Keywords Ionosphere, Ion drift, Electric field, Data quality

Graphical Abstract

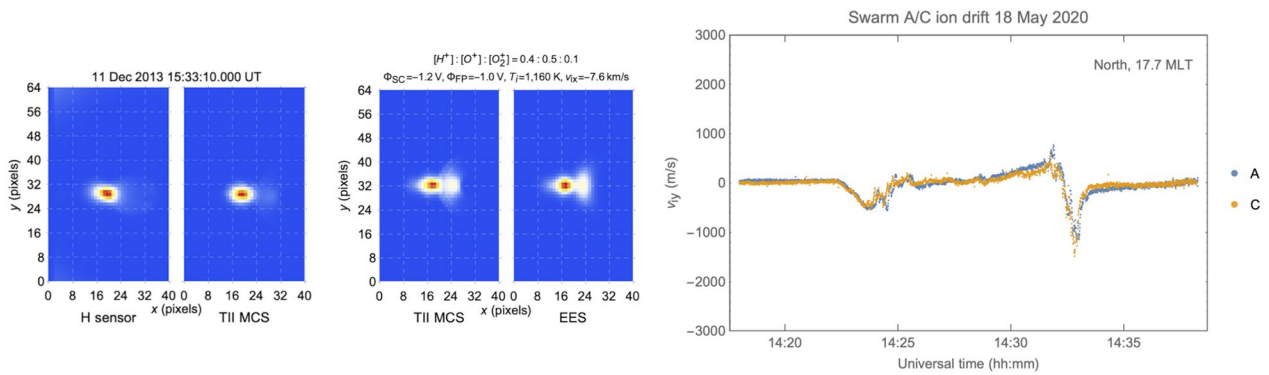

*Correspondence:
Johnathan K. Burchill
jkburchi@ucalgary.ca
Full list of author information is available at the end of the article

Introduction

In this paper we assess the Swarm Thermal Ion Imager (TII) measurement performance. The TII is an innovation in space plasma instrumentation pioneered for the European Space Agency's Swarm satellite mission (Olsen et al. 2004; Friis-Christensen et al. 2008; Knudsen et al. 2017). Swarm's scientific objectives include the study of magnetic fields generated within the Earth's core, crust and mantle, as well as of electric currents flowing in the ionosphere and magnetosphere, and associated forcing of the upper atmosphere. Measurements of the "external" magnetic and electric fields and plasma are relevant to topics that include auroral electrodynamics, electromagnetic energy and momentum flow, particle acceleration and heating, ionosphere–thermosphere coupling, and plasma physics. The TII was designed primarily to measure ion bulk drift velocity $\vec{v}_i$, ion temperature, and the component of electric field $\vec{E}_\perp$ perpendicular to the geomagnetic field $\vec{B}$ obtained from

$$\vec{E}_\perp = -\vec{v}_i \times \vec{B}, \tag{1}$$

under suitable assumptions (Knudsen et al. 2017). This method for calculating electric field is commonly used, notably with the retarding potential analyzer and ion drift meter package flown on Dynamics Explorer 2 and the Defense Meteorological Satellite Program series of satellites and recently developed for the ICON mission (Heelis et al. 2017, and references therein). Launched in November of 2013, Swarm is in its ninth year of operations and the TIIs continue to provide measurements beyond the original 4-year mission lifetime.

Ion imaging as a method for measuring core and suprathermal ionospheric plasma was developed in Canada in the late 1980s and early 1990s for the cold plasma analyzer on the Swedish Freja satellite (Whalen et al. 1994; Lundin et al. 1998). The first sounding-rocket-borne electro-optical charged-particle imagers (the Suprathermal Ion Imager and Thermal Electron Imager) were flown on GEODESIC (Knudsen et al. 2003; Burchill et al. 2004) and subsequently on several more sounding rockets including Cusp-2002 (Burchill et al. 2010) and Joule II (Sangalli et al. 2009; Burchill et al. 2012). A boom-mounted suprathermal electron imager (which included an ion imaging mode) was developed at the University of Calgary for the Canadian Cassiope satellite ePOP payload (Knudsen et al. 2015), now operated by ESA as Swarm Echo.

The sounding-rocket-borne and ePOP sensors were deployed on stiff booms 50- to 100-cm-long with instrument boxes located on the platforms. The Swarm TII sensor heads are housed directly inside an electronics box affixed to the front of the satellite rather than on booms. Each entrance slit accommodates rammed ion flow within a planar field of view. The TIIs were developed in the mid-to-late 2000s at COM DEV Ltd. (now Honeywell Canada) in consultation with the University of Calgary through Canada's membership in the European Space Agency's Earth Explorer Programme.

The Swarm mission comprises three identical satellites (Swarm A, B, and C) in near-polar, near-circular low-Earth orbits at altitudes of approximately 460 km (A and C) and 530 km (B). Swarm A and C are maintained in close proximity to one another, with A following C by 4 s to 10 s, and with a separation of 1.4° in the right ascension of their ascending nodes. Each satellite is equipped with precision magnetometers and an Electric Field Instrument (EFI), in addition to other instrumentation not central to this study. Each EFI consists of two orthogonally oriented TIIs attached to a planar faceplate, and two spherical Langmuir probes. The faceplate is biased negatively with respect to the satellite chassis to attract ionospheric ions and repel ionospheric electrons to mitigate the effect of positive satellite charging. The instrument paper by Knudsen et al. (2017) has additional details on the EFI. In the "TII principle of operation" section, we describe the TII measurement principle as it relates to this study.

Low-energy plasma (LEP) measurements in space pose many significant challenges stemming from the fact that the measured population is easily disturbed by relatively small potential variations, both within the instrument and in the highly disturbed environment created by a supersonically moving spacecraft. Nearly all previous LEP instruments have relied on integral measurements of rammed ion flux, using the retarding potential analyzer technique to obtain along-track velocities and temperatures, and the ion drift meter for cross-track velocities (e.g., Hanson and Heelis 1975). In contrast, the TII sensors on Swarm are the first satellite-borne instruments to provide detailed images of the core ion distributions in the energy range from less than 1 eV (corresponding to a temperature of 11,600 K) to more than 10 eV, thereby providing a detailed view of a variety of non-ideal behaviors that can arise.

A chief aim of our paper is to quantify the realistically achievable measurement performance of a Swarm TII. This will establish a context within which actual measurement performance may be interpreted. Indeed, ESA's Earth Observation Programme sets a high standard for metrology. ESA has required the instrument provider to develop an end-to-end instrument simulator (EES)—prior to launch—principally to assess the capability of the proposed technique to meet mission measurement requirements.

We note analogous efforts undertaken to characterize the ICON Ion Velocity Meter (IVM) measurement performance (Heelis et al. 2017) prior to launch, which included methods of simulation under the anticipated range of measurement conditions at low latitude. The EES developed for the present study represents a different approach. We surmise that the space physics community may derive insight and inspiration from the comprehensive analysis of error sources that was undertaken for the Swarm TII. The methodology and results of the investigation for the Swarm EFI, with a focus on the TII, are described in the "Theoretical TII measurement performance" section. Our study may be seen to address, if in part, the titular problem raised by Storey (1998): "What's wrong with space plasma metrology?"

Within the scope of the Swarm mission, level 0 data are timestamped packets of uncalibrated scientific and monitoring signals represented in engineering units. Level 1b measurements are calibrated physical measurements from a single instrument. Selected intervals of Swarm level 1b ion drift measurements have been available to the scientific community since 2014, and they have since featured in various discoveries (e.g., Pakhotin et al. 2021; Wu et al. 2020; Pakhotin et al. 2020; Miles et al. 2018; Archer et al. 2017; Park et al. 2017; Wu et al. 2017; Park et al. 2016; Juusola et al. 2016; Zou et al. 2016; Archer et al. 2015). The first datasets were processed by an operational level 1b processor prototyped by the University of Calgary in collaboration with the Swedish Institute of Space Physics (IRF) and implemented by ESA. The operational processor was designed to be operated daily for the entire mission — without human intervention — and included automatic estimation of some TII calibration parameters. In practice these processors did not perform as intended for reasons discussed below. Major revisions to the TII data reduction algorithms and datasets grew out of ESA's annual Swarm calibration and validation workshops, culminating in the current experimental TII cross-track ion drift processor. The most recent dataset, version 0302 used here, covers the Swarm mission from December 2013 through late 2021.

Validation of data products requires comparison with the "truth", often determined with an independent measurement, and the validity of earlier Swarm TII datasets has been studied to some degree. A comparison of cross-track ion drift with signal associated with the co-rotating ionosphere and satellite yaw showed good agreement (Knudsen et al. 2017). Knudsen et al. (2017) examined velocity resolution (equivalent to sensitivity) and electric field resolution using several months of observations drawn from the satellite commissioning period in early 2014. The velocity resolution was estimated to be of order 10 m/s (2σ) at electron concentrations greater than 10^4 cm^{-3}, consistent with TII measurement requirements.

Ionospheric flow and temperature are measured by ground-based radars, though typically at much lower spatial resolution than is achieved in situ, and with much longer integration periods. Fiori et al. (2016) compared level 1b ion drifts from the original level 1b processor with drifts derived from the SuperDARN coherent scatter radar network statistical potential model and found overall agreement at large scales. A more recent SuperDARN study compared radar line of sight and vector drift measurements with Swarm cross-track ion drift (Koustov et al. 2019), finding significant correlation in the independent measurements, but with radar values being lower by 40% on average. Lomidze et al. (2019) reported overall agreement to within 200 m/s (r.m.s.) between TII cross-track drifts and cross-track ion drifts derived from the empirical Weimer 2005 electric potential model for the subset of the mission from November 2015 to June 2017 available at the time (dataset version 0201). That model in turn is based on 18 months of data from the RPA/IDM instruments on the Dynamics Explorer II mission in the mid-1980's. Statistical flow patterns showed clearly expected behavior in both the northern and southern hemispheres under different interplanetary magnetic field conditions. Two notable characteristics of the latter three studies are the validation of morphological flow features such as the high-latitude convection reversal boundary and the prevalence of more spatial/temporal structure and larger flow magnitudes in the Swarm ion drift time series than is seen in the various radar measurements and empirical models.

Ion temperature, which the TIIs are also designed to measure, has proven difficult to derive from raw measurements due to various anomalies having origins both internal and external to the instrument. There is certainly evidence in the data that the TIIs respond to variations in ion temperature (e.g., $T_{\mathrm{iy,H}}$ in Figure 9d of Knudsen et al. 2017). Yet the focus on TII processing has been on ion drift and electric field; consequently, ion temperature flight measurements are not discussed further in this paper.

Another aim of our paper is to provide guidance on the interpretation of the published Swarm TII ion drifts. To this end, in the "Swarm TII flight performance" section, we describe anomalous properties of the ion imagery, such anomalies having causes either outside or within the TII sensors. In the "Ion drift velocity" section, we provide an assessment of the ion drift quality by showing examples and statistics from the most recent level 1b dataset spanning

approximately 8 years. This paper concludes with a discussion and summary of the findings.

TII principle of operation

Figure 1a and b shows examples of imagery from the first orbit of operation following high-voltage commissioning of the Swarm C EFI. For a detailed description of the TII electrostatic analyzer, see "Knudsen et al. (2017)". TII imagery is available from ESA's Swarm TRACIS product version 0101. Each pair of panels show the horizontal (H) and vertical (V) sensor images obtained simultaneously. The x and y coordinates refer to TII sensor frames as shown in the lower-left part of Fig. 1 of Knudsen et al. (2017) with increasing ion energy corresponding to lower values of x. Signal level represents ion count rates formed by the electrostatic energy-per-unit charge and direction of arrival analyzer (consisting of outer and inner dome-shaped electrodes) and mapped by an electro-optical detection system onto a charge-coupled device (CCD). Each sensor has a slightly different optical center arising from manufacturing tolerances. The inner dome electrode is biased negatively by an amount sufficient to focus the dominant ion species O^+ into a bright spot (i.e., the brightest signal in each panel of Fig. 1). The low-intensity ring of signal to the right of the O^+ spot is hypothesized to be H^+. As discussed below, some features of TII imagery arise from satellite–plasma interactions, while others originate within the sensor. Details of the distribution of ion energies and angles of arrival have been indispensable in understanding measurement performance.

All such images are obtained at a rate of 16 per second, one pair of which are telemetered to ground at preset intervals from several seconds to several minutes. The remainder of the images are reduced onboard as described below. Ions are analyzed when high-voltage is applied to the electro-optical stack. This stack consists of two microchannel plate (MCP) intensifiers in a chevron configuration coupled to a phosphor-coated fiber-optic taper (Knudsen et al. 2017). During normal TII science operations the imagery is processed by onboard software, and the resulting level 0 measurements and instrument monitoring data are sent to the ground as so-called LP &TII instrument source packets (ISPs).

Processing of ion imagery consists first of subtracting a constant threshold (of order 100 DN, but different for each EFI and occasionally updated throughout the mission) from each pixel value and clipping negative values to zero to remove background or low-intensity spurious signals from the imagery. The result is multiplied by a sensor-specific gain correction map (the TII gain map). Due to constraints on telemetry bandwidth imposed at the satellite level, images are reduced onboard, and only a subset of full imagery is transmitted to ground. Details of the image reduction algorithm are provided in Knudsen et al. (2017), the result of which is a set of zeroth, first and second moments computed along the CCD y coordinate (in a direction approximately perpendicular to the satellite velocity vector) at a cadence of two each per second per sensor, as well as first moments along both CCD coordinates at a cadence of sixteen each per second per sensor. The various moments are the basis for estimating ion drift and ion kinetic temperature.

In the original level 1b processing scheme, the zeroth moments, or column sums, represent a proxy for ion flux as a function of kinetic energy; these were used to distinguish the major ion species, assumed to be atomic

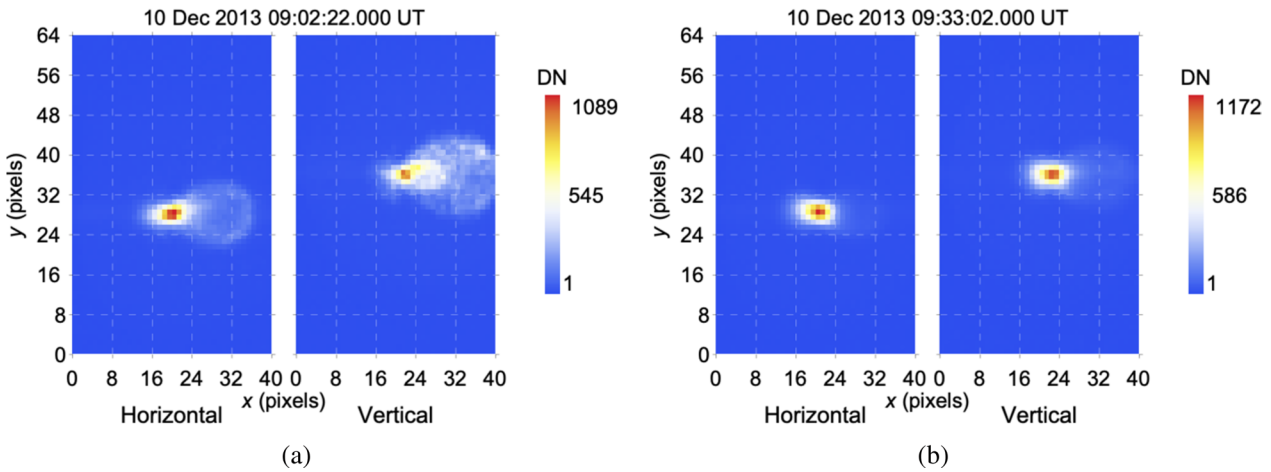

Fig. 1 Swarm C TII images from the first operation. (**a**) First images with both sensor high voltages at operational levels. (**b**) Best focused images from the first orbit. Data number or "DN" refers to analog-to-digital converter output. See Knudsen et al. (2017) for details regarding the formation and interpretation of images

oxygen ions, from the minor ion species (assumed to be protons) by fitting a double Maxwellian curve to the profiles. This approach was abandoned following the appearance of various unanticipated behavior (anomalies) that intermittently introduced large artifacts in the level 1b products. All such image properties and the subset of full images are available in level 0 packet data. Full images from one or the other sensor can be obtained at a rate of one per second in a dedicated calibration mode that is used primarily for characterizing pixel-to-pixel gain variations. The instrument can be placed in a "ready state" mode in which all TII high-voltage power supplies are switched off.

Theoretical TII measurement performance

ESA's Swarm mission was steered by a Mission Advisory Group consisting of experts tasked with establishing instrument performance requirements consistent with mission science goals. Measurement requirements for the EFI TIIs are listed in Appendix A. The requirements associated with determining quantities within prescribed random error limits on scales from global (one orbit) down to 10 km effectively represent orbit-averaged measurement accuracy (i.e., average systematic error). Requirement R-EFI-41 for electric field measurement resolution is interpreted herein to correspond to random errors on small scales (up to 35 km).

EFI prime contractor COM DEV consulted the University of Calgary's EFI team about sources of uncertainty in the TII ion drift, electric field, and ion temperature measurements. Error sources studied prior to launch broadly consisted of detector noise, manufacturing errors, satellite-induced effects, plasma-induced effects, and calibration uncertainties. Methods of estimation were based on analysis, laboratory measurements, and end-to-end simulations. In this section, we describe methods of estimation, the end-to-end instrument simulator (EES), and lab tests performed to characterize measurement performance ahead of the launch.

Methods

Methods for estimating errors vary according to the error source and are listed in Table 1. Details are provided in the following sections.

Analysis

Much of the pre-launch investigation involved Monte Carlo modeling of TII imagery using an ion trajectory tracer developed at the University of Calgary. This model, called the TII MCS, satisfied the requirement to provide realistic simulations of ion imagery within the constraints of certain assumptions about the form of the ion velocity distribution and satellite–plasma interactions, thus allowing development of an instrument simulator model and level 1b processor, and supporting the investigation of error sources associated with the proposed image analysis approach. The TII MCS may be considered part of the level 1b processor insofar as it was used to generate an interpolation table of ram ion drifts and temperatures parameterized on image properties (see Appendices C and D). Following the launch of the Swarm satellites, the TII MCS has aided the interpretation of actual flight TII imagery to assess possible origins of various imaging anomalies.

The TII MCS model consists of: an accurate specification of the nominal TII analyzer geometry and electrode voltages; a finite-difference Laplace numerical solver, based on the successive over-relaxation technique, for calculating the electrostatic field within the sensor; a random number generator based on the rejection method (Press et al. 1992) for specifying initial ion positions and velocities at the TII entrance aperture from a specified bi-Maxwellian velocity distribution for each ion species;

Table 1 Error sources and estimation methods. (EES) end-to-end simulation; (A) analysis; (M) measurement

Error source	A	M	EES
Particle counting noise			X
MCP pulse height noise			X
CCD dark noise			X
Total detector noise		X	X
Faceplate bias noise			X
Aperture misalignment		X	
Inner dome bias noise		X	X
End-to-end detector gain variations	X		X
Angular misalignment	X		
Thermal de-centering	X		
Solar UV contamination		X	
Automatic gain control	X		
Charge-transfer inefficiency	X		
Satellite attitude control			X
Satellite attitude errors			X
Satellite velocity	X		
Satellite position	X		
Satellite potential			X
Satellite sheath (thin approximation)			X
Magneto-torquer field	X		
Minor ions			X
Galactic cosmic ray events			X
Atomic hydrogen ions			X
Electric field fine structure (16 Hz)			X
Geomagnetic field errors	X		
Transfer function truncation			X
Transfer function coefficient calibration errors	X		X

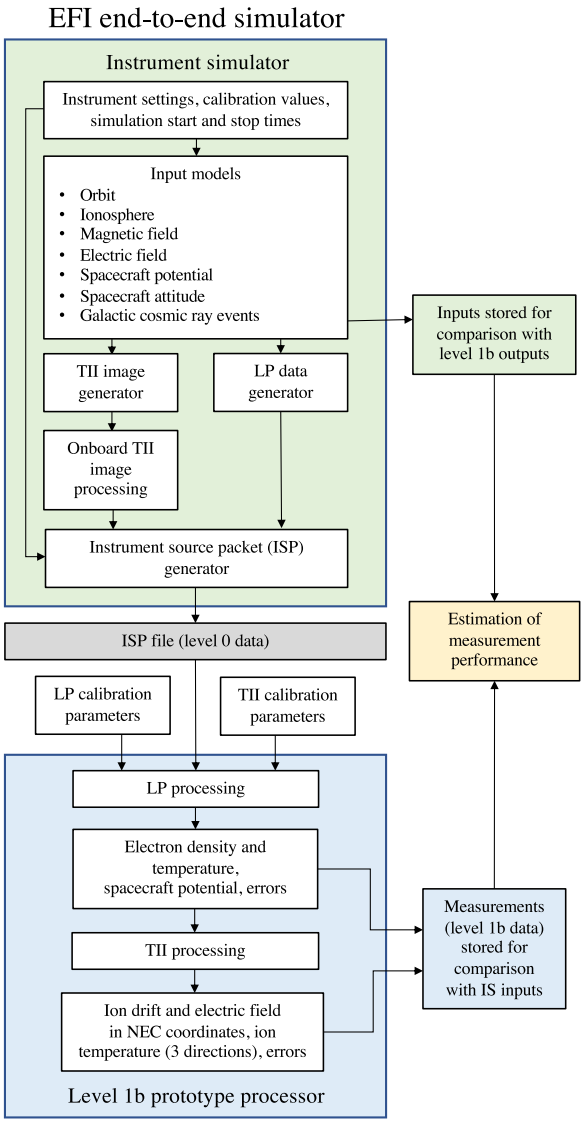

Fig. 2 Schematic overview of the Swarm EFI EES. The EES consists of the instrument simulator (top), the prototype level 1b processor (bottom), and an error estimation module (right)

and a Runge–Kutta–Fehlberg particle tracer (Galassi et al. 2009) for calculating detector count rates. The relationship between an ion's initial kinetic energy per unit charge and the ion's radial position at the detector is illustrated in Fig. 3 of Knudsen et al. (2017). The TII MCS returns the number of ions within each pixel per integration period. These count rates are scaled to match those expected for the given plasma conditions. The more particles that are traced, the less noisy are the resulting images at the expense of additional computing time. Gain and noise characteristics associated with the electro-optical detection system are added to the TII MCS images in the EES described below.

Measurement

Lab measurements were carried out at the University of Calgary's Space and Atmospheric Instrumentation Laboratory (SAIL) in support of COM DEV's test program. The SAIL facility has supported many space flight hardware developments, including sounding rocket and satellite low-energy ion instrumentation. Swarm TII development and pre-flight test campaigns made use of two high-vacuum chambers. The main chamber, a cylinder approximately 1 m in diameter by 1 m long, comprises a CryoTorr-10 cyrogenic pump, an oil-based roughing pump, a robotic two-axis translation and two-axis rotation table, an Oxford Applied Research Lion-50 ion source, a 300 W Cermax LX-300UV xenon bulb ultra-violet lamp, and a UV flat-field integrating sphere source. All ion beam and UV flat-field tests were performed in this chamber. A smaller chamber was used for detector preparation, including slowly raising voltages on new MCP and phosphor components and extracting (burning in) the initial $\sim 1\,\mathrm{C\,cm^{-2}}$ of charge density from the MCPs. The small chamber was routinely operated at $\sim 10^{-8}$ Torr base pressure and the large chamber was typically operated at levels of 10^{-7} Torr to 10^{-6} Torr.

End-to-end instrument simulation

We define end-to-end instrument simulation to mean the generation of synthetic measurements using realistic input parameters (e.g., instrument modes and settings, plasma properties, orbital parameters, etc.) combined with models of the instrument's operation on a satellite together with the scientific processing of the data to assess measurement performance, taking into account all significant sources of uncertainty and their correlations. End-to-end simulations provide insight into the relative contributions of a priori-determined error sources. The simulator is designed to be a faithful approximation to a real instrument in orbit. Error sources are incorporated using physical or empirical models.

Figure 2 illustrates the EES approach taken for the EFI TIIs. An instrument simulator module combines models of the instrument, the satellite, and the plasma and field environment to produce a file containing the level 0 instrument data (in the form of ISPs). A level 1b processor module calculates ion drift, electric field, ion temperature, error estimates and quality flags from the ISPs and instrument calibration parameters. The Swarm EFI EES was implemented in Matlab by the University of Calgary in collaboration with the Swedish Institute of Space Physics who developed the ISP and Langmuir probe modules. Simulated level 0 and level 1b data also served as reference datasets for validating the operational level 1b processor developed by ESA.

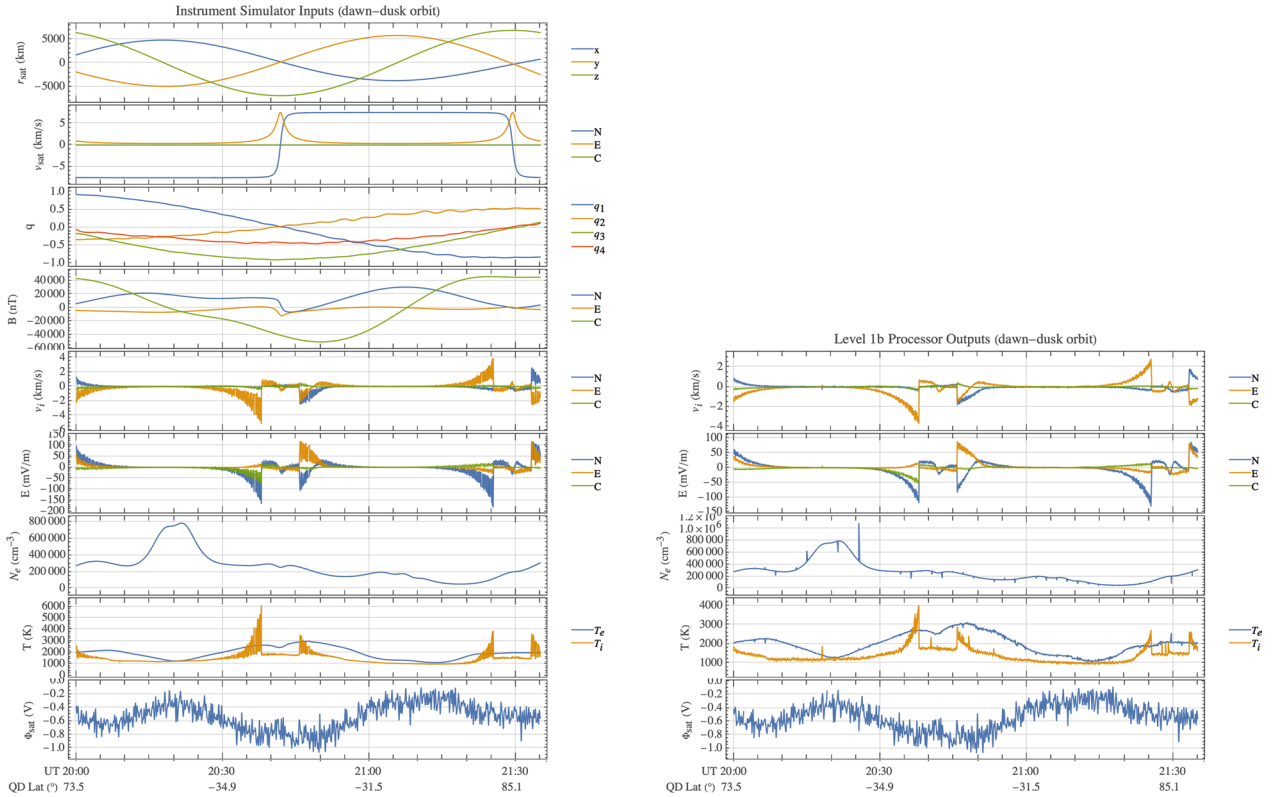

Fig. 3 Level 0 and 1b outputs of the EES. **a** Example model outputs (16 Hz) from the EES for a dawn–dusk orbit at 530 km altitude. From top to bottom: satellite position, satellite velocity, satellite attitude quaternions, magnetic field, ion velocity, electric field, electron concentration, electron and ion temperatures, and satellite potential. **b** Example level 1b outputs (2 Hz) generated by processing data corresponding to the example at left. From top to bottom: ion velocity, electric field, electron concentration, electron and ion temperatures, and satellite potential

Figure 3a illustrates the EES model inputs for a dawn–dusk orbit at 530 km altitude, the nominal initial altitude of Swarm B. Starting from a specification of start and stop times and other simulation options, the EES uses phenomenological, or notional, models for (referring to the panel labels in Fig. 3a) satellite position r_{sat}, satellite velocity v_{sat}, quaternions q specifying satellite attitude (orientation), and high-latitude electric field E. Empirical models are incorporated for magnetic field B (using the Swarm End-to-End Magnetic Field Industrial Package; e.g., Olsen et al. 2004), ionospheric plasma composition (not shown), density N_{e} and temperature T for ions and electrons (using the International Reference Ionosphere 2003, or IRI; e.g., Bilitza and Reinisch 2008), and galactic cosmic ray flux (not shown, using a model specified by ESA). Ion drift velocity $\vec{v}_{\mathrm{i}}$ is derived from the electric and magnetic fields as an E-cross-B drift. A model developed by IRF is used to simulate satellite potential Φ_{sat}. From such inputs the EES generates ISPs.

Figure 3b illustrates the corresponding key EES products generated from those ISPs by the level 1b processor module. Shown from top to bottom are the vector ion drift in north, east, center (NEC) coordinates (see Appendix B for a description of coordinate systems), the vector electric field, electron density, ion and electron temperatures, and satellite potential. Error sources are studied in isolation and in combination using separate simulation runs.

Because generating TII images with sufficient particle numbers can take many hours with a Monte Carlo-based tool like the TII MCS, simulating 16 images per sensor per second over a full orbit (corresponding to 182,400 images) was not feasible. Instead, two-dimensional Gaussian models in cylindrical coordinates (consisting of radius and azimuthal angle in the detector plane) were fit to TII MCS image intensities using the method of nonlinear least-squares for a set of one-time simulated images spanning the domains of ion species, drifts, temperatures, and satellite floating potentials anticipated for Swarm. The resulting Gaussian model

coefficients were fit with multi-dimensional polynomials of varying degrees, depending on the desired accuracy of the representation. These so-called instrument simulator transfer functions were then used to generate approximate TII images according to specified input parameters, facilitating rapid full-orbit end-to-end simulations. Details of the TII image model transfer functions are provided in Appendix C, including a visual comparison in an example showing TII MCS and EES imagery.

Each simulation consisted of two runs of 5700 s each (one orbit) in separate dawn–dusk and noon–midnight circular orbits. The dawn–dusk orbit passes through the geographic center of a model South-Atlantic Anomaly (SAA) at 315° E longitude. Most simulations were conducted for an altitude of 530 km (the upper altitude of the Swarm satellites) to assess worst-case signal-to-noise levels and light-ion effects. The effect of molecular ions on the TII performance was estimated from a simulation at 300 km altitude (corresponding to late mission), where such ions appear in greater concentration. To cover a greater domain of parameter space than provided by the ionospheric model (IRI), additional simulations were performed with plasma densities scaled by constant factors, and ion temperatures enhanced through an ad hoc frictional ion heating model. We note a distinction between end-to-end instrument simulation as performed in this study and end-to-end mission simulation described by Olsen et al. (2004), whose purpose was to assess errors in core magnetic field model recovery from synthetic measurements for different orbital configurations of spacecraft spanning the full Swarm mission.

"LP &TII Science" ISPs are the main input to the level 1b prototype processor (Knudsen et al. 2017). Image moments representing positions and widths of the O^+ ion signal are related to ion total kinetic energy per unit charge and ion temperature via transfer functions. These transfer functions were derived from a parametric study of modeled image moments over a broad range of plasma parameters. Given the total kinetic energy E_i of the O^+ signal and the sensor-to-plasma floating potential Φ_F, the ion speed is obtained from

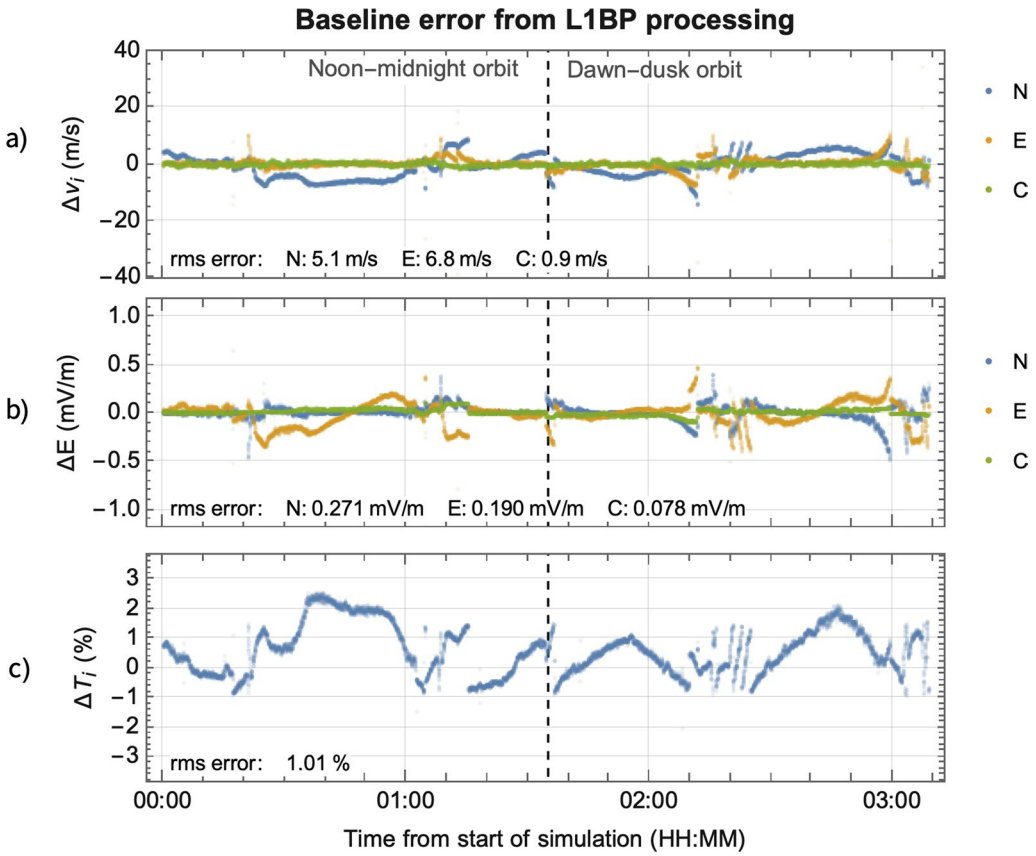

Fig. 4 Residual (baseline) EES errors for **a**) ion drift, **b**) electric field, and **c**) ion temperature represent the best attainable level 1b performance when known error sources are not included. Vector components are labeled N (north), E (east), and C (center). The noon–midnight and dawn–dusk simulations are shown together with the transition between the two orbits marked by dashed lines

Table 2 Orbit-averaged EFI TII errors (1-sigma) estimated using the EES

Error type	Error source / simulation conditions	v_i (m/s)			E (mV/m)			T_i (%)
		N	E	C	N	E	C	
Baseline	Level 1b processing	5.1	6.8	0.85	0.27	0.19	0.078	1.0
Random	Instrument and platform noise	2.5	1.3	1.1	0.043	0.081	0.023	0.27
	Particle counting noise, $n_{e,IRI}/10$	0.16	0.16	0.15	0.0056	0.0063	0.0026	0.034
	MCP pulse height noise	1.4	1.2	1.1	0.038	0.048	0.020	0.28
	CCD dark noise	0.12	0.13	0.11	0.0043	0.0043	0.0021	0.024
	Inner dome bias voltage noise	0.13	0.056	0.050	0.0019	0.0041	0.0011	0.014
	Faceplate bias noise	2.0	0.39	0.013	0.016	0.065	0.011	0.008
	Satellite potential noise	0.21	0.029	0.001	0.0012	0.0051	0.0007	0.001
	Attitude noise (0.003° RMS)	0.13	0.19	0.18	0.0063	0.0054	0.0031	0.025
	Attitude noise (0.125° RMS)	1.0	5.6	5.8	0.18	0.11	0.096	0.000
	GCR noise (with SAA)	2.4	2.0	1.9	0.031	0.048	0.033	0.75
	GCR noise (without SAA)	0.31	0.26	0.22	0.0087	0.012	0.0029	0.092
Systematic	20% residual detector gain depletion	34	17	2.8	0.67	1.2	0.23	16
	Electric field fine structure (16 Hz)	7.8	15	1.9	0.56	0.37	0.17	0.80
	Non-O^+ ion contamination, 530 km	36	13	1.3	0.54	1.4	0.23	4.2
	Non-O^+ ion contamination, 300 km	14	7.3	1.1	0.31	0.52	0.12	1.9
	GCR events (with SAA)	51	7.2	5.9	0.10	0.56	0.21	17
	Satellite rotation	0.94	1.3	1.1	0.046	0.039	0.021	0.26
	Satellite floating potential	3.7	0.64	0.020	0.028	0.14	0.016	0.022
	CCD dark noise	5.4	1.3	0.54	0.053	0.17	0.030	3.2
	Simplified transfer functions	12	3.8	0.12	0.16	0.46	0.084	8.2
Total	Resolution (530 km altitude)	3.4	1.4	1.2	0.051	0.11	0.026	0.42
	Accuracy (530 km)	30	28	6.3	1.0	1.2	0.36	4.6
	Accuracy (300 km)	28	30	7.7	1.3	1.2	0.43	3.5
	Accuracy (530 km with ion heating)	31	28	6.5	1.0	1.2	0.38	4.6

$$v_r = \sqrt{\frac{2q(E_i + \Phi_F)}{m_{O^+}}}, \tag{2}$$

where $m_{O^+} = 2.66 \times 10^{-26}$ kg and $q = 1.602 \times 10^{-19}$ C are the per-particle mass and charge of ionized oxygen ions. Three-dimensional velocity vectors are reconstructed from v_r and the azimuthal positions of the ion signal from the orthogonal TII sensors. Vector measurements of ion drift velocity and electric field are represented in an inertial coordinate system positioned at the satellite with unit vectors pointing in the local geographic north (N), east (E), and center (C) directions (Knudsen et al. 2017). The level 1b prototype processor can generate error estimates using separate error transfer functions and error propagation, although these were not included in the performance study. Details of the level 1b transfer functions can be found in Appendix D.

Higher measurement accuracy can be achieved with higher-order transfer functions. This would require, however, a very large number of independent and accurate measurements of ion drift and ion temperature to which the transfer functions could be fit. Laboratory calibration of the transfer functions was considered and deemed not feasible due to difficulties in faithfully reproducing in a calibration facility the plasma environment and its effect on the satellite Debye sheath. Instead, a set of in-flight calibration procedures were developed for the Swarm mission. Owing to the limited availability of independent measurements, from ground-based incoherent scatter radars for example, during the 4-month in-flight commissioning phase, just the four most significant terms in these transfer functions were retained for level 1b processing of ion kinetic energy, and three terms each for the orthogonal ion temperatures. Errors associated with these truncations were estimated by analyzing end-to-end simulations using the full and truncated transfer functions.

Figure 4 illustrates the character of the level 1b measurement errors when full transfer functions are used, and all known error sources, other than those inherent to the data processing, are disabled. The resulting differences between outputs and inputs represent the minimum errors attainable with this processing technique and are

referred to as the baseline errors. These baseline errors are reported in each panel of Fig. 4 (and in the first entry in Table 2). They are calculated as the root-mean-square (RMS) difference between EES inputs and outputs for the two simulation orbits after averaging to the Nyquist frequency of 1 Hz and removing 30 s from the beginning of each orbit to allow time for the TII automatic gain control to stabilize. Each panel's abscissa represents time in hours and minutes from the beginning of the combined simulation. The noon–midnight orbit is shown first, and the dashed vertical line indicates the start of the dawn–dusk orbit.

Some processing considerations that affect the measurement accuracy include: approximating the O^+ signal with a Gaussian model; widening of the column profiles due to co-adding of successive images between which plasma parameters have changed; and calculating the radial position of the O^+ signal from reduced image data, instead of calculating it directly from the images. This simulation serves as a baseline against which simulations of all other error source simulations are assessed. Excellent measurement performance is obtained in this best case, with ion drift RMS systematic errors of 5 m/s, 7 m/s and 1 m/s in the N, E and C directions, respectively, corresponding electric field RMS errors of 0.3 mV/m (N), 0.2 mV/m (E) and 0.08 mV/m (C), and RMS ion temperature error of 1%. The largest ion drift errors occur where the flow shear (from the input model) is largest (e.g., for the N and E components near 02:15 in Fig. 4, corresponding to 20:40 UT for the dawn–dusk orbit of Fig. 3b).

Experience with flight data has shown that, due to the intermittent appearance of unanticipated imaging artifacts (anomalies) and external influences described below, the prototype level 1b processing algorithm does not consistently provide robust measurement and error estimates. A different processing approach is now used with a focus on estimating the cross-track ion drift and its random error, along with quality flags, on account of the cross-track ion drifts being much less susceptible to anomalies than the along-track drifts in practice. Ion temperature measurements are particularly susceptible to imaging anomalies and are not currently provided as a data product. In lieu, a recently released physics-based model incorporating Swarm EFI LP electron temperature and density measurements and a neutral atmosphere model (NRLMSISE-00) provides estimates of ion temperature (Lomidze et al. 2021). Appendix E summarizes the processing status of the TII-related Swarm data products.

The level 1b prototype processor module nevertheless represents a useful tool for analyzing instrument simulations to assess the contributions of known sources of error to the TII measurement performance. In the following sections, we examine the orbit-averaged random, systematic, and total RMS errors shown in Table 2. Errors are typically reported to two significant figures. Detailed plots showing time series of individual error sources and total error are provided in Appendix F.

Random errors

The combined effect of all random error sources on the measurements, under the condition of stationary input signal, determine the measurement resolution for each quantity. The EES was used to estimate random noise for which all systematic error sources (described in the next section) were disabled. The results are listed in Table 2 as "Random" errors. To calculate the random error for each quantity, two simulations were carried out (one in a noon–midnight orbit and one in a dawn–dusk orbit passing through the SAA) for the specified error source and conditions, and the differences between EES inputs and outputs were downsampled to the Nyquist frequency (1 Hz). The baseline level 1b processing error was subtracted. Results from both orbits were concatenated into one time series. To approximate stationary inputs, a high-pass filter was applied to the measurement errors consisting of a half-Gaussian rejection band with a peak at 0 Hz having a full-width-at-half-maximum of 0.2 Hz to exclude variations on timescales slower than about 5 s. This removes most residual systematic errors, which are particularly large, in comparison with random errors, near strong reversals in the high-latitude electric field. Outliers more than five standard deviations from the time series mean, also typical of systematic error near strong reversals in the electric field, were removed. A 30-s interval was discarded from the filtered result at the beginning of each orbit to remove artificial discontinuities associated with bootstrapping the TII automatic gain control model. In effect, the random error for a given measurement quantity was estimated as the RMS statistic of filtered differences between EES outputs and inputs from the noon–midnight and dawn–dusk orbits combined.

Errors in vector ion drift and electric field quantities are provided in the North–East–Center (NEC) inertial coordinate system. Ion temperature is the average of the four temperature estimates corresponding to the along-track and cross-track directions for each sensor. Ion temperature error is presented in relative terms.

Instrument and platform noise

The first entry for random error shows the case for all instrument and platform sources enabled. The maximum ion drift error is in the northward component (2.5 m/s); its magnitude is well within the 10 m/s (2σ) measurement resolution requirement. The next seven entries in

Table 2 show the magnitudes of the individual instrument and platform error sources.

Particle counting noise

The EES implements particle counting noise (i.e., Poisson or shot noise) as a random component proportional to the square root of the TII pixel intensity prior to detection at the MCP. Associated fluctuations are proportional to the square root of the reciprocal plasma density. Shot noise was estimated for cases of nominal IRI plasma density (not shown) and also at one-tenth IRI plasma density to encompass the lower bound of the required density range. Even at densities as low as 10^4 cm^{-3}, TII MCS simulations predict ion counts in the vicinity of the O^+ peak greater than 10,000 per integration period, making particle counting noise a negligible source of error. EES simulations confirm that particle counting noise is negligible compared to the 10 m/s (2σ) requirement at ion densities above 10^4 cm^{-3}.

MCP pulse height noise

The TII sensors differ from most space-borne charged-particle detectors in that they do not "count" individual particles. A microchannel firing generates a pulse of electrons, the height of which follows a normal distribution at high gain and an exponential distribution at low gain, each distribution having mean G (i.e., gain). Net charge is accumulated in the CCD in what is known as analog operation. An automatic gain control circuit (AGC) sets the target MCP voltage to keep the CCD signal level within limits suitable for maintaining sufficient signal-to-noise ratio of the ion spot (corresponding to peak TII pixel intensity of ∼200 DN) without saturating the CCD output amplifier (corresponding to a pixel intensity of ∼1800 DN). In this paper DN refers to the digitized output (digital number) of the binned CCD pixels. Large particle fluxes result in reduced MCP gain which places its operation well into the exponential pulse-height regime.

During flat-field characterization prior to launch, using a UV-integrating sphere to illuminate the entire TII sensor imaging area, MCP output current was 0.03% of strip current during image saturation, which is much less than the typical 5% maximum required to maintain MCP linearity. This is quite different from particle counting instruments, where each individual MCP firing must be detected individually, and is a significant advantage of the CCD-based detector technique. See Knudsen et al. (2003) for a discussion of the noise characteristics of analog MCP operation. An exponential pulse-height distribution, with scale factor $1/G$, was used in the EES as a worst-case estimate of MCP noise. MCP pulse height noise represents the largest error for the cross-track (E and C) ion drift components (the N and C components of electric field), and is the largest contributor to ion temperature random error.

CCD dark noise

CCD dark noise was modeled as a normally distributed Poisson noise based on operation at 10° C with a corresponding dark background signal dependent on the sensor temperature having a value typically around 10 DN. This level is consistent with observations from CCD bench testing made at 20 °C. EES simulations show that dark noise is a negligible source of random error.

Power supply noise

Measured inner dome deflection voltage shows a maximum excursion of 25 mV across the range of operating temperature, and a corresponding 2σ random error of 18 mV. A value of 25 mV (2σ) is used in the EES, and resulting errors are negligible. Faceplate bias noise, which is the noise level of the faceplate power supply, was modeled in the EES at a level of 10 mV/m (2σ) based on preflight measurements by COM DEV. Faceplate bias noise represents the largest source of instrument and platform error in the northward component of ion drift and correspondingly in the eastward component of electric field.

Platform noise

The main sources of platform-related errors are uncertainties in satellite floating potential and the satellite attitude. The random error in floating potential as estimated by the LP will show up predominantly in the along-track direction, which corresponds mainly to geographic north–south except at very high latitudes. The EES ion drift error for this source is about 0.2 m/s, primarily in the N component as expected. Attitude measurement uncertainty is modeled using an RMS measurement uncertainty of 0.003° in each axis of roll, pitch and yaw. This level was estimated recently from attitude time series at several epochs of the Swarm mission. The errors are largest in the E and C directions as expected and are negligible. At ESA's direction, the attitude error was originally modeled at a worst-case RMS level of 0.125° per axis, about two orders of magnitude larger than observed in practice, corresponding uncertainties in the E and C components of ion drift of about 6 m/s. This is shown as a separate entry in Table 2 and is not included the instrument and platform noise entry.

Galactic cosmic ray events

An empirical model of galactic cosmic rays in the South-Atlantic anomaly and polar regions was used to investigate the effect of penetrating radiation on the CCD output signal owing to interactions of energetic particles

with the CCD crystal substrate. Cosmic ray events were chosen randomly from a set of simulated CCD images provided by ESA and added to EES images at a rate that depends on latitude and proximity to the SAA and polar regions. The SAA part of the model was excluded from the final performance metrics on the basis that measurements from a CCD detector in this region would be considered outliers which can be readily identified by geographic location. The "without SAA" entry in Table 2 retains the polar galactic cosmic ray model.

GCR events represent an external noise source and are therefore not included the total instrument and platform noise entry in Table 2. Total GCR events give rise to ion drift noise levels of 2 m/s and ion temperature noise levels of about 0.7%. Excluding the SAA, orbit-averaged ion drift errors from GCRs are 0.2 m/s to 0.3 m/s and ion temperature errors are less than 0.1%.

Measured TII velocity resolution

The effect of detector noise on ion signal position was measured before launch with the flight EFIs using an argon ion beam source. Tests were conducted at beam energy settings of 25 eV, 30 eV, 35 eV, and 40 eV for rotations of the instrument within the detector plane with respect to the ion beam direction of −20°, −10°, 0° (normal incidence), 10°, and 20°. Onboard processing generated 16 Hz first image moments for 2 min at each rotation angle. For Swarm C EFI horizontal TII sensor tests performed on 18 December 2010, median ion beam density was $9.9 \times 10^3\,\mathrm{cm}^{-3}$. Across all beam configurations the median standard deviation in signal position moments is $[\Delta x, \Delta y] = [0.0093, 0.0049]$ pixels (after scaling to 1 Hz by dividing by 4), which is equivalent to $[\Delta v_x, \Delta v_y] = [5.6, 2.9]\,\mathrm{m/s}$, noise levels that are comparable to the Instrument and Platform noise modeled by the EES. The average EES density for the "particle counting noise" entry in Table 2 was $3.1 \times 10^4\,\mathrm{cm}^{-3}$ with concomitant noise levels of 0.16 m/s. This scales to 0.29 m/s RMS at the equivalent median lab ion beam density, which is negligible in comparison with measured noise. A significant part of measured noise is likely associated with variability in the laboratory ion beam energy rather than sources within the TII sensor. Beam energy is determined by a bias voltage set by the ion source controller. This voltage cannot be measured directly but is displayed on the controller at a resolution of 0.1 V, whereas variations of order 0.01 V would explain the observed excess variability.

Systematic errors

A similar approach to the one described above to model random errors was used to assess TII systematic errors, which determine measurement accuracy. Systematic sources affecting accuracy are shown in Table 2. In each case the sum of baseline error and random error was subtracted from the raw differences, and no high-pass filtering was performed. Error sources that are accounted for in instrument calibrations (e.g., aperture parallelism errors) are not included in the instrument simulator.

Detector gain depletion

Characterizing detector response to a uniform source (flat fielding) was accomplished in the lab with a mercury lamp (Analamp BHK 80-1025-01) and a UV-integrating sphere with a 10-cm-diameter aperture. The uniform beam exiting the integrating sphere shines through a quartz window in the Swarm chamber, down a short arm (10 cm diameter, 10 cm long), and onto the 2.5-cm-diameter detector surface. Beam uniformity was not tested. The manufacturer's specification shows the dominant and shortest-wavelength output line at 253.7 nm. MCP technical data indicate poor response above 100 nm however the MCPs had a strong response to this lamp. It was found that flat-field estimates using this lamp could correct the TII sensor gain variations to a level of 5% or better. Humidity exposure experiments carried out prior to launch revealed strong increases in MCP gain after exposure to humidity, with a slow return to baseline gain in regions of the detector exposed to ion signal. It was estimated that prolonged exposure to high fluxes of ions following launch could result in uncorrected regions of gain variation at levels of up to 20%. Such gain depletions are modeled in the EES by applying a normalized, Gaussian-shaped gain depletion to simulated TII images using the form

$$G = 1 - \delta e^{-((x-x_0)^2+(y-y_0)^2)/2\sigma^2}, \tag{3}$$

with a worst-case $\delta = 0.2$. The parameters characterizing the gain depletion position (x_0 and y_0) and width (σ) are estimated from the average of 10,000 EES TII images on normally distributed ion drift velocities with standard deviations of 100 m/s in the along-track and cross-track directions. Uncorrected gain variation is one of the largest sources of systematic error in ion drift, electric field, and ion temperature.

Electric field fine structure

The effect of fine-scale spatial variations in electric fields (equivalently ion drift), corresponding to Doppler-shifted variations at frequencies greater than 2 Hz, was investigated using a model of normally distributed random electric field fluctuations at 16 Hz. The amplitude of the variations was set to 20% of the electric field magnitude. The fluctuations appear in the EES only at high latitudes. Fine structure was found to represent a minor source of

systematic error, primarily in the along-track direction for ion drift.

Non-O^+ (minor) ion contamination

The influence of minor ions on the error budget was estimated using International Reference Ionosphere concentrations of ions (six species) at both 530 km and 300 km altitude. In each case, simulations were performed with and without minor ions using the full TII transfer functions. At 530 km the main non-O^+ ion is H^+. Below 300 km in the IRI model N^+ and molecular ions become significant. Systematic error from minor ions at 530 km is considerable; minor ion contamination at 300 km is much less so.

GCR events

GCR events rates are sufficiently high near the peak of the SAA that they can lead to large systematic errors in along-track ion drift (and cross-track electric field) and ion temperature. Outside the SAA, GCRs act as a random noise source and produce negligible systematic error.

Satellite rotation

Satellite attitude control is maintained in part by magnetorquers, which use pulses of electric current to generate magnetic moments through which the geomagnetic field imparts additional angular momentum to the satellite depending on the sign and magnitude of the current pulse. The magnetic field generated by the magnetorquers imparts a small change to the velocity of the incoming ions via the Lorentz force. Using field values estimated by ESA for a maximum expected magnetorquer current of 0.1 A, the maximum ion drift error magnitude is 18 m/s worst case and 12 m/s (1σ) averaged over position. The expected mean magnetorquer current of 17.1 mA gives an average ion drift error of 2.1 m/s (2σ). The EES does not contain a time-series model of the magnetorquer operation, but it includes a slowly varying attitude model based on spline interpolation of random control points for satellite roll, pitch and yaw with amplitudes up to 4° from the nominal orientation. Attitude measurement uncertainty was modeled as a random error and was therefore not included for this case. Systematic errors associated with attitude variation are of order 1 m/s for ion velocity and less than 0.3% for ion temperature.

Satellite floating potential

The satellite floating potential error was estimated using a Langmuir probe simulator developed by IRF and incorporated into the EES with an option to disable LP-related errors. Distortions of ion drift from the satellite plasma sheath were modeled using a thin-sheath approximation and were accounted for in the level 1b TII transfer functions. Dedicated particle-in-cell simulations have shown that the sheath can distort the ion distribution functions resulting in 50 m/s velocity errors in cases where the plasma density is less than 10^3 cm^{-3}, or the ion temperature exceeds 0.5 eV (Marchand et al. 2010). Such conditions are never met in the IRI model on which performance requirements were based and are thus not included in the EES. Uncertainty in the satellite floating potential leads to small errors primarily in the N component of ion drift and E component of electric field.

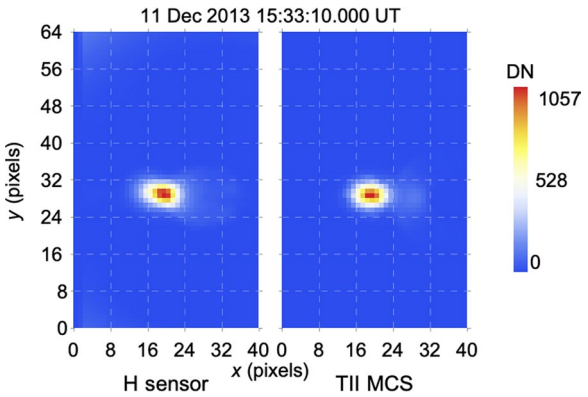

Fig. 5 Swarm C H sensor image (left) and TII MCS model (right): 11 December 2013 at 15:33:10 UT. Model parameters: 85% O^+, 15% H^+, $T_{ix} = 0.12$ eV, $T_{iy} = 0.05$ eV, $v_x = 7000$ m/s, $v_y = 350$ m/s, $v_z = 0$ m/s, $\Phi_{S/C} + V_{FP} = -1.47$ V. The satellite was traveling southward at a latitude of about −45°

CCD dark noise

CCD dark noise includes a background pixel level corresponding to dark current and depends on detector temperature. Dark current is treated in the on-board processing of TII images by subtracting a pre-determined constant 10 DN. Even small amounts of residual dark noise above this level lead to systematic errors in the image moments corresponding to a moderate uncertainty in the northward component of ion drift (5 m/s) and a substantial uncertainty in ion temperature (3%).

Simplified transfer functions

As described in Appendix D, the TII transfer functions comprise multi-dimensional polynomials that relate measured image properties (e.g., the O^+ spot position and width corresponding to the primary ion signal peak)

Table 3 Measured angular errors for an azimuthal scan of a laboratory ion beam

Commanded azimuth	Measured signal position and 2σ errors
−20°	−20.06 ± 0.50°
−0°	0.028 ± 0.36°
+10°	−10.28 ± 0.28°
+20°	−19.64 ± 0.42°
+27°	−26.41 ± 0.50°

to ion parameters (e.g., the ion ram energy and temperature). The higher the orders of the transfer function polynomials (i.e., the greater the number of coefficients in the model), the more accurately the ion parameters can be retrieved from the image properties. As it was not practical to calibrate transfer functions (using lab or in-flight data, or with a validated TII MCS image simulator) containing dozens or hundreds of coefficients, a set of truncated, or simplified, transfer functions were developed using several coefficients each, for which calibration against known characteristic of ion drift and temperature was deemed feasible, at the expense of increased measurement uncertainty. For the EES a sufficiently large set of low-noise simulation images were used in constructing the model transfer functions to eliminate least-squares fitting errors as a source of systematic instrument error. The effect of truncating the transfer functions is seen largely in the along-track ion drift (i.e., the N and to a lesser extent E components), and in the E component of electric field. This effect is a significant source of ion temperature systematic error.

Errors in the higher-order coefficients depend on the accuracy of the TII MCS, which was not easy to assess prior to flight. Validation of the TII MCS could be carried out by comparing images with flight TII imagery for a collection of incoherent scatter radar overflights, where radar estimates of plasma parameters serve as inputs to the TII MCS. To illustrate the comparison of flight imagery and model imagery (but not for an ISR overflight), Fig. 5 shows an early Swarm C H sensor image from 11 December 2013 along with a TII MCS model image using nominal instrument settings. Simulation parameters were chosen to give a qualitatively good reproduction: ion composition of 85% O^+ and 15% H^+, bi-Maxwellian ion temperatures of $T_{ix} = 1400\,\mathrm{K}$ and $T_{iy} = 600\,\mathrm{K}$, ram ion drift velocity components of $v_x = 7000\,\mathrm{m/s}$, $v_y = 350\,\mathrm{m/s}$, and $v_z = 0\,\mathrm{m/s}$, and the sum of the spacecraft floating potential and EFI faceplate bias voltage of $\Phi_{S/C} + V_{FP} = -1.47\,\mathrm{V}$. The satellite was traveling southward at a speed of ~7,600 m/s near a geographic latitude of about −45°. The difference between the satellite speed and the inferred ram ion speed implies a northward ion drift of ~600 m/s in a reference frame co-rotating with the Earth. The TII MCS captures basic features of the image, including the O^+ signal and a faint plateau of H^+ to its right, although the detailed shapes of these populations are difficult to reproduce with the TII MCS, and the apparent large northward flow (600 m/s) and strong temperature anisotropy ($T_{ix}/T_{iy} > 2$) implied by the simulation parameters are unexpected at this latitude. A comprehensive validation of the TII MCS should take into account realistic Debye sheath structure, ISR plasma parameter estimates, LP spacecraft potential estimates, and TII detector gain inhomogeneities. This would be a significant undertaking beyond the scope of the present investigation.

Other systematic errors

Other systematic errors were assessed and deemed either to be negligible or not feasible to implement in the EES. Satellite velocity errors, as determined by GPS receivers to be less than 1 m/s, are negligible, as are satellite position errors, which are less than 100 m. Calibration-related errors arise mainly from uncertainties in the detector origin within the imaging plane (i.e., the center of symmetry of the optical system projected onto the CCD), uncertainties in the direction cosine matrices that transform measurements from a TII reference frame to the satellite reference frame, and uncertainties in TII transfer function coefficients.

The thickness and position of the TII entrance aperture largely determines the shape and extent of the O^+ spot on the detector. Non-uniformity in the thickness of the aperture can therefore lead to a systematic distortion of the measured ion signal azimuthal position. This effect was studied experimentally. Table 3 shows commanded sensor azimuth with respect to a constant 30 eV ion beam and the corresponding ion spot azimuthal position for the Swarm EFI engineering model sensor. The differences between measured spot azimuth and commanded azimuth are consistent with a systematic azimuthal error of less than 0.26°, corresponding to a cross-track velocity error of less than 34 m/s (1.7 mV/m). It is assumed that such constant errors can be removed using in-flight calibrations.

Angular misalignment characterizes errors related to thermally induced sensor distortions of the angle between CCD rows and the satellite x axis (approximately aligned with the satellite velocity vector). The magnitude of the effect is of order 0.14° or 18 m/s in the cross-track directions (0.9 mV/m). Thermal strains of the analyzer detector center were modeled and the resulting

displacement was found not to exceed 3.1 microns, with a 2σ equivalent displacement of 2.2 μm, or 0.006 image pixels. Using a velocity sensitivity of 6 m/s per 0.01 pixels gives an error of 3.6 m/s (0.24 mV/m).

Various environmental effects were analyzed. To assess the effect of solar ultra-violet contamination, the TII entrance slits were illuminated with the Cermax xenon bulb reflecting off of a cold mirror to remove infrared and shining through a quartz window in the SAIL chamber. The output UV flux of about 150 W/m^2 near 250 nm to 390 nm is about 70% of the solar flux in the same wavelength range. Each sensor was rotated with respect to the fixed source through the sensor's field of view. The effect of UV on TII imagery was initially found to be significant due to scattering from reflecting surfaces within the sensor. The sensor geometry was subsequently modified, including the addition of a baffle within the entrance aperture, to remove the effect of UV. Based on the experiments confirming suitable rejection of UV at levels comparable to the solar irradiance at Earth, contamination from EUV (such as by geocoronal H-Ly-α) is expected to be negligible despite the higher quantum efficiency of the MCPs at shorter wavelengths. Errors in magnetic field measurements on Swarm are less than 0.5 nT, and the resulting error in electric field estimates is negligible (Eq. 1).

Charge-transfer inefficiency errors, which result in smearing of the CCD image as it is shifted toward the readout register, were modeled to be of order 1.5 m/s at end of life (4 years), and are considered negligible for ion drift and electric field. Charge-transfer inefficiency does affect ion temperature at a level of 2%. However, these errors were predicted to develop slowly over the lifetime of the mission, and were assumed to be able to be compensated with temperature transfer function updates. Errors associated with step changes in the TII automatic gain control settings were found to be negligible in simulations.

Total error

The remaining rows of Table 2 show EES estimates of total measurement resolution (at an altitude of 530 km) and accuracy (at altitudes of 530 km and 300 km) with all EES error sources active, including truncated transfer functions and 20% gain depletion, for the IRI parameter space, but excluding the effects arising from the South-Atlantic Anomaly.

The EES predicts measurement resolution for ion velocity of 3 m/s RMS in the N component and less than 1 m/s in the E and C components based on internal noise sources. Electric field measurement resolution is of order 0.1 mV/m RMS in the N component and smaller in the other components. Ion temperature measurement resolution is predicted to be 0.4% RMS.

In estimating total accuracy we have subtracted the orbit-averaged mean difference for each quantity prior to calculating RMS values with the assumption that DC offsets can be determined during the mission using an accumulation of incoherent scatter radar measurements during Swarm flybys. The IRI-based EES does not cover the 0.1 eV to 1.0 eV (1160 K to 11600 K) ion temperatures specified in the Swarm requirements. To assess TII performance over this range, we have included for the 530 km case a simulation that incorporates an ad hoc ion frictional heating model based on the magnitude-squared of the ion drift. Theoretical ion drift measurement accuracy is of order 30 m/s in the N and E components and 6 m/s in the C component. Electric field accuracy is 1 mV/m in the N and E components, and 0.4 mV/m in the C component. Ion temperature accuracy is better than 5% at both altitudes.

Swarm TII flight performance

All Swarm EFIs were powered on for the first time on 2 December 2013, following which several days were designated for commissioning the Langmuir probes. TII high-voltage supplies were then commissioned starting with Swarm A on 8 December 2013. All units were commissioned by 11 December 2013, and the TIIs were operated more or less continuously for much of the first year of the mission. For most of the mission, however, the TIIs have generated measurements at a reduced duty cycle of typically several to ten orbits per day (out of about fifteen orbits per day) as a means to slow and reverse the occurrence of several sensor imaging anomalies that became apparent only after launch.

Initial operations were conducted with a phosphor voltage setting of 4000 V and the MCP front voltage was initially maintained around −1400 V to −1500 V by the TII automatic gain control. The inner dome voltage on all sensors was set to approximately −60 V. The official commissioning phase of the mission continued until mid April 2014, during which various tests were carried out to characterize optimal EFI operating parameters. In addition, an extensive calibration campaign was carried out, which included satellite attitude maneuvers to calibrate coordinate systems and timing, and inner dome voltage sweeps to characterize the TII gain maps. An operational calibration processor, designed to provide statistically significant refinements to the TII transfer function coefficients and detector coordinate origins by fitting a model to the mission history of O^+ image moments, was found to be too sensitive to anomalous image features to be effective and was ultimately shelved. Significant effort, both operational and analytical, has

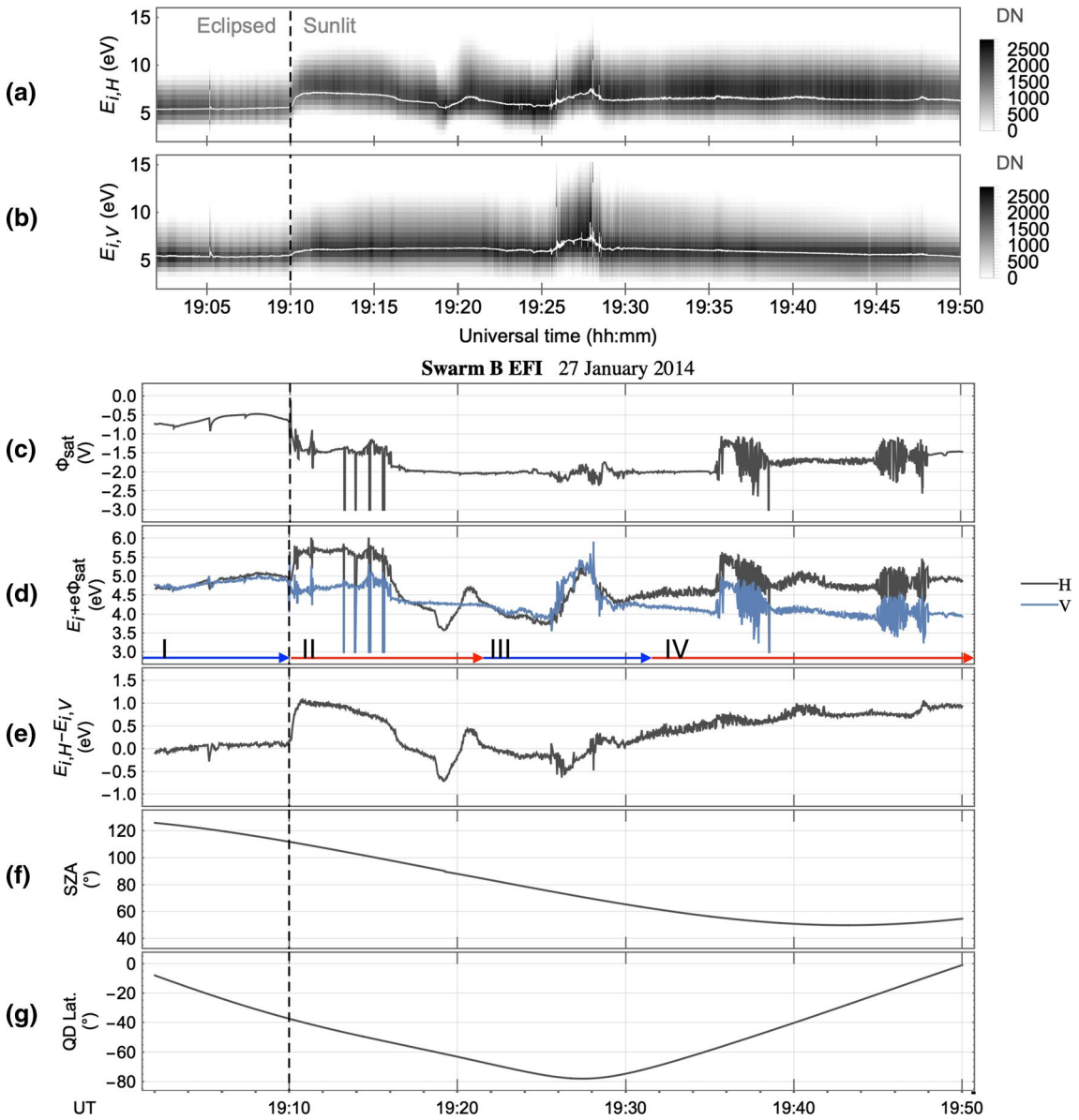

Fig. 6 Swarm B TII energy spectra for the horizontal sensor (**a**) and vertical sensor (**b**) on 27 January 2014. White lines show the 16 Hz first *x*-moments averaged to 2 Hz and converted to ion ram energy using Equation 4. Satellite floating potential estimated from the LP (**c**) is used to estimate the ion ram energies (**d**) beyond the electrostatic sheath as measured by the horizontal (black) and vertical (blue) sensors. The solar zenith angle at the satellite (**e**) is used to identify the period of eclipse, and the quasi-dipole magnetic latitude (**f**) illustrates the position and motion of the satellite in the southern hemisphere

gone into estimating each sensor's gain correction map as it evolves on orbit, which has proven challenging, and which will be described in a separate publication. Various onboard image processing parameters have been adjusted throughout the mission, including a transition from − 60 V to − 100 V of the inner dome bias in mid-2018 (at the end of Swarm's initial 4-year mission) to focus the main O^+ spot onto a less-exposed region of each detector.

We begin our examination of the TII measurement performance with an analysis of a case study of ion ram energy in the "Ion ram energy" section. This case illustrates the rationale for abandoning the operational level 1b TII data processor in favor of a cross-track ion drift processor. The "TII imaging anomalies" section provides an overview of numerous unexpected features of the TII measurements, particularly with respect to the quality of the ion imagery. Much of the TII imagery

is anomaly-free. No attempt is made to provide a full account of occurrence locations, root causes, or efforts at automated quality control, all of which are ongoing topics of investigation. Full imagery is generated by the instrument at a pre-set cadence of one image pair every few minutes during the early part of the mission, and later routinely at intervals from 8 to 30 seconds. The imagery can inform the assessment of level 1b measurement quality; we therefore review the kinds of anomalies seen in the level 0 imagery. In the "Ion drift velocity" section, we present examples of the quality of the ion drift and electric field measurements available in the 0302 TII cross-track ion drift dataset, and provide some brief statistics on measurement resolution and variability.

Ion ram energy

The H and V TII sensors on a single satellite should measure approximately the same ion ram kinetic energy. Displacement of the O^+ signal in the along-track direction (with energy increasing from right to left in the TII imagery shown in this paper) can arise from variations in along-track ion drift, satellite velocity, satellite floating potential, faceplate voltage relative to the satellite chassis, and ion composition. Both sensors should be sensitive to these effects in the same way, since each sensor pair uses a common inner dome voltage and automatic gain control algorithm. Non-zero flow angles (relative to the spacecraft x axis) may give rise to relative variations in measured ram energies. This is expected to be a negligible effect except at very large flow angles. Direct measurements of ion ram energy from the horizontal and vertical sensors should differ by the induced e.m.f. in the polar regions (the TII entrance apertures have a cross-track separation of 7.4 cm), or by at most 0.03 eV. The top two panels of Fig. 6 reveal an unexpected behavior, however, with measured ion ram energies from the two sensors differing by up to 1 eV.

These energy spectrograms are derived from level 0 column sums (Knudsen et al. 2017) calculated onboard from gain-corrected imagery. We used the TII MCS to calibrate the relationship between CCD pixel along-track position i and ion ram energy E_i (in eV) and obtained the relation

$$E_i = 1.21 \times 10^{-3}(i - i_0)^3 - 3.09 \times 10^{-2}(i - i_0)^2 + 0.744(i - i_0) - 2.4, \quad (4)$$

where i_0 is a real number offset that represents the projection of the origin of the energy analyzer on the CCD. The column sum magnitudes represent detector count rates and are shown in gray tones as illustrated with the intensity scales at the right in Fig. 6. Time variations in intensity are due to the several-second response time of the automatic gain control to variations in input ion flux. The white lines represent the first x moments calculated onboard at 16 Hz, averaged to 2 Hz and converted to ion ram energy using Equation 4. The remaining panels represent (c) satellite floating potential at the location of one of the spherical probes, as derived from the LP harmonic mode (Knudsen et al. 2017), (d) ion ram energy corrected for the satellite floating potential, (e) the difference between the H and V sensor energy measurements, (f) solar zenith angle at the satellite, and (g) quasi-dipole magnetic latitude. The faceplate voltage was set to 0 V relative to the satellite chassis for the entire interval. We have ignored the e.m.f. induced by satellite motion in this analysis. Negative spikes to − 14.3 V in the satellite floating potential estimate are clipped in Fig. 6c.

Figure 6 illustrates a conundrum regarding the interpretation of ion ram energy measured by the two TII sensors, which is that at times both sensors show similar profiles in ion energy (intervals marked I and III in panel

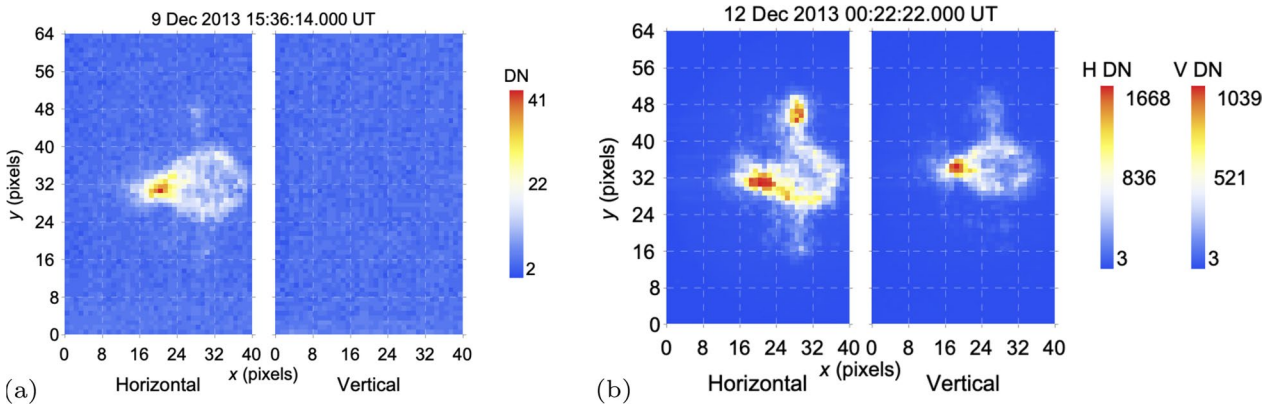

Fig. 7 Swarm B examples of the angel's wing anomaly from raw imagery. (**a**) The anomaly first appeared on 9 December in the H sensor within 10 s of the first high-voltage imaging operations. (**b**) A clear example with angel's wings appearing simultaneously in both sensors a few days later

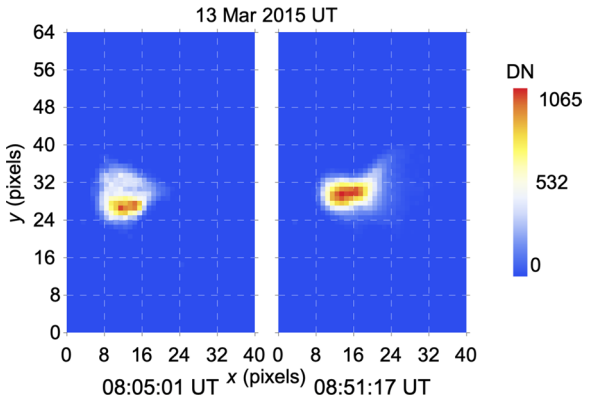

Fig. 8 Gain-corrected image of a bifurcation anomaly from Swarm A from 13 March 2015. Left panel: bifurcation of nominal ion peak associated with apparently larger kinetic energy (shift of peak to the left) than normal. Right panel: gain-corrected image obtained ~46 min later showing no evidence of bifurcation in the same region of the detector, ruling out gain depletion or other detector anomaly as the root cause of the bifurcation

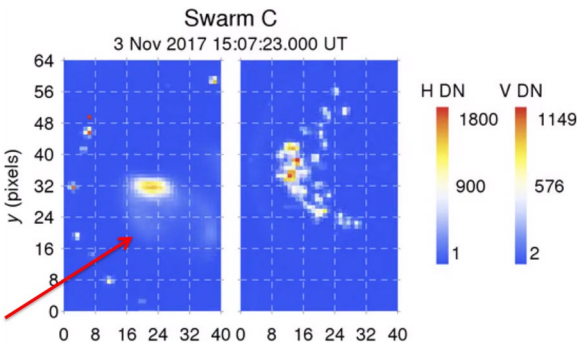

Fig. 9 Classic wing anomaly (red arrow) and peripheral anomalies (islands of concentrated signal in the left panel) in raw Swarm C horizontal TII imagery (left panel) on 3 November 2017. The noisy signal at right (vertical sensor) is associated with low input flux

(d), and at other times there are large differences (intervals II and IV), and that the different timescales over which the differences occur suggest different anomalous processes are at play. At the other times, the two sensors in effect exhibit different and time-varying sensitivities to the plasma environment.

As the satellite descended into the southern hemisphere it passed from eclipse into sunlight at 19:10 UT (dashed line). This transition was associated with a rapid decrease in estimated satellite potential, seen also as an increase in ion ram energy. The charging physics is not straightforward due to competing effects of solar-generated satellite photoelectrons and ionospheric photoelectrons, background plasma concentration, solar panel charging, and constraints on particle motion by the geomagnetic field. Note that the horizontal and vertical sensor spectra vary differently in response to the change in satellite potential, and ram energies differ by up to 1 eV over large intervals (panel d). The spikes and high noise in the corrected energies evidently arise from anomalies in the satellite potential estimates from the LPs. In interval IV the H sensor ion energy measurement is somewhat noisier than the V sensor measurement, and the two estimates diverge slowly during the ascending part of the pass.

To account for possible scenarios where one sensor is less reliable than the other, the original TII level 1b processing had a weighting factor for deriving along-track ion drift from either one or both of the sensors. In practice, however, it is not clear which sensor provides the more accurate estimate at any given time. We note that large errors in measured ram energy give rise to large non-geophysical variations in the along-track ion drift and cross-track electric field, and consequently in the north and east components of these vectors in the NEC frame, depending on the latitude of the measurement.

Such variations in ion apparent ram energy occur sufficiently often as to render the automated operational level 1b and calibration processors largely ineffective. This motivated us to develop robust ion drift estimation based on the cross-track measurements which are less susceptible to satellite charging and sheaths. The result was the development of the TII cross-track ion drift processor and datasets (Burchill and Knudsen 2020), examples from which are provided below in the "Ion drift velocity" section.

TII imaging anomalies

An imaging feature termed "angel's wings" was observed from the very start of the mission in Swarm A and B TII operations. The first occurrence of angel's wings for the Swarm B horizontal sensor occurred within 10 s of applying high voltage, as shown in Fig. 7a. Figure 7b shows images from 12 December 2013 in which the features appear simultaneously in both sensors. Angel's wings appeared somewhat later in Swarm C imagery. The onset of angel's wings happened well before any other signs of imaging degradation, yet they were not observed during laboratory testing nor in sounding rocket flights and are thus hypothesized to be caused by factors exterior to the sensor such the plasma sheath or exposure of the satellite to sunlight. Swarm's solar panels include a network of wiring between cells that can present some exposed potentials to the surrounding plasma. To minimize these effects, solar panels were grounded at the forward-facing side of the satellite, with potentials increasing aftward, making it unlikely that electrostatic disturbances could propagate to the forward location of the EFI in

the supersonic flow. The effect of angel's wings on the original level 1b processing, as well as the simplified cross-track ion drift processing, is observed in both ion drift and ion temperature. A revised on-board processing approach implemented in 2018 removes much of their influence using carefully constructed gain maps to aggressively crop areas of unwanted signal. As of the publication date of this paper the cause of angel's wings is still under investigation.

Another unexpected image feature evidently having an external cause is the "bifurcation" anomaly (Fig. 8). Shown are gain-corrected Swarm A TII images from 13 March 2015. Both images are from the horizontal TII sensor. In the left-hand panel the main O^+ spot is split into an upper and a lower part. Forty-six minutes later, there is no evidence of bifurcation in the same detector region, thus indicating that dip in signal on the left-hand panel is not associated with an imperfect detector gain correction, i.e., the sensor detects two ion beams at its entrance aperture. Other examples (not shown) appear to show a "hole" in the main spot, although they can occur at low latitude where ion drifts are not strong enough to drive non-Maxwellian velocity distributions such as "donuts" (e.g., St-Maurice and Schunk 1979), and they are not associated with transverse acceleration of ions (e.g., Chang et al. 1986). Like angel's wings, such intra-spot structures, particularly those observed at low latitude, are possibly manifestations of satellite–plasma interaction processes.

Various other anomalies evidently originate from processes within the TII sensor. The "classic wing" anomaly refers to the sometimes broad, low-intensity plateau shown by the arrow in Fig. 9. This feature was seen early in the mission on all sensors and may be related to imperfect gain corrections, whereby the low-intensity tail of the ion energy distribution is imaged with much higher count rates in comparison with the main peak due to relatively lower sensitivity the region of the central ion spot. Gain variations as great as -90% have been observed, and these can vary on timescales of orbital periods to days. This effect is greatly mitigated through a program of daily rest and sensor scrubbing cycles (flooding the sensor with a broad low-energy ion beam, using small inner dome bias voltages) tailored to each satellite. The depths of the gain depletions appear to have stabilized in recent years. The scrubbing referred to here is a defocusing of the ram ion beam onto to the MCP operated at maximum gain. Based on review of flight data during scrubs, the ions do not cover the full MCP, particularly near where the MCP is mechanically supported at its perimeter. The ions do cover, however, the entire region from which moments are calculated. While helpful, on-orbit scrubbing is not an optimum method of maintaining detector performance.

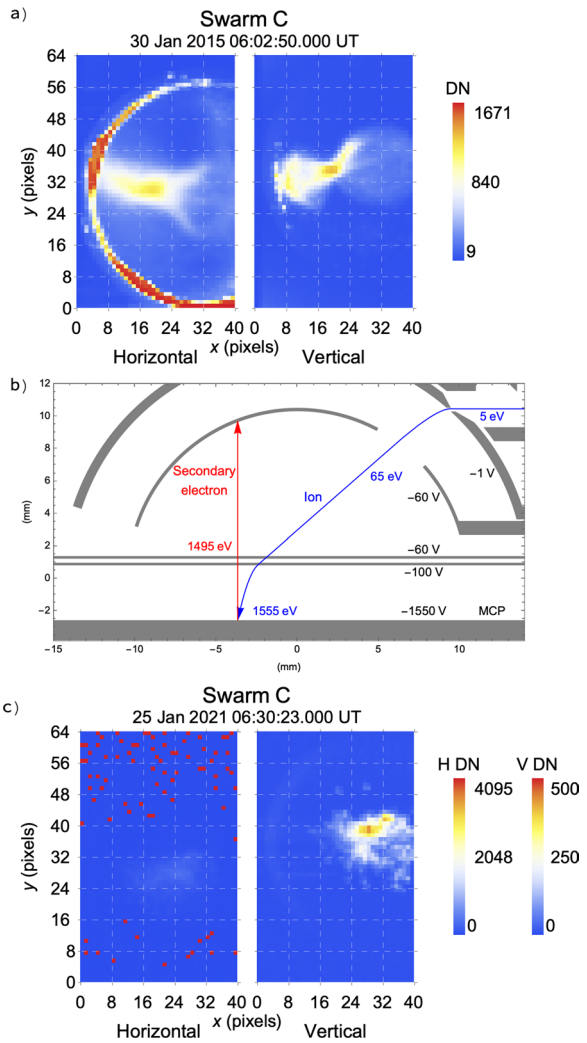

Fig. 10 (**a**) Swarm C TII example of the ring anomaly, appearing as a bright arc and defocusing of the rammed ion spot, particularly evident in the left-hand panel. (**b**) Illustration of secondary electron feedback from the input surface of the MCP. Electrode voltages are labeled in black, ion kinetic energy in blue, and electron kinetic energy in red. (**c**) The "measles" anomaly consisting of quasi-randomly distributed pixel count rates of 4095 DN

There are indications, based on in-flight experimentation showing worse imaging performance during periods of elevated sensor temperature, that the rapid variation of gain (on timescales of tens of minutes or longer) is connected with redistribution of water vapor and condensation within the sensor, as well as exposure of the microchannel plates to the neutral background of predominantly atomic oxygen. The presence of water vapor in the instrument was anticipated during instrument development and was investigated by exposing

Table 4 TII imaging anomaly occurrence probabilities from analysis of full images obtained during science operations

Satellite	Swarm A		Swarm B		Swarm C	
TII image pairs	3657029		3477460		2904328	
TII sensor	H	V	H	V	H	V
Upper angel's wing	0.556	0.593	0.453	0.440	0.349	0.215
Lower angel's wing	0.194	0.413	0.366	0.320	0.096	0.311
Bifurcation	0.006	0.025	0.013	0.027	0.003	0.020
Classic wing	0.120	0.105	0.117	0.140	0.086	0.108
Peripheral	0.377	0.283	0.243	0.388	0.326	0.170
Measles	0.000	0.000	0.000	0.000	0.009	0.000

test sensors to air at 1 atm and different humidity levels to simulate the last phases of the launch campaign during which no dry nitrogen purge line was available. It was decided during the design phase that various methods of sealing the detector or incorporating heaters were solutions not feasible. One consequence of humidity exposure, revealed by the controlled humidity cycling tests, is variation in detector gain observable at the low ion source fluxes then available to the test program. Analysis and further testing carried out prior to flight demonstrated adequate recovery through detector scrubbing in vacuum using a UV source, and the proposed use of gain correction maps to be derived at monthly intervals from in-flight gain calibrations. Analysis involving image simulations and UV flat-fields obtained in the lab showed that uncorrected gain variations of up to 20% could be corrected to a level that would meet TII uncertainty requirements.

Detector exposure on orbit to ion flux levels several orders of magnitude greater than those used in the laboratory appear to cause a significant and dynamic redistribution of water within each sensor. Islands of concentrated signal around the periphery of the raw image in Fig. 9, termed "peripheral" anomalies, are potentially due to feedback of secondary MCP electrons accelerated back up towards the inner dome by the large negative bias on the MCP front plate, ionizing pockets of water vapor trapped at the bottom of the inner dome. The resulting ions can be accelerated back towards the MCP, thereby creating additional signal for the CCD. A similar feature, the "ring" anomaly shown in Fig. 10a, first appeared only after many months of operation on orbit. It and the associated defocusing of the main O^+signal are also hypothesized to be caused by scattering of MCP feedback electrons by analyzer electrodes. This effect, illustrated in Fig. 10b with measured electrode voltages for the image in Fig. 10a and an assumed incident ion kinetic energy of 5 eV, will be investigated in a separate study. Figure 10c shows an example of yet another anomaly termed "measles" evidently associated with the CCD output amplifier or digitizer or onboard image binning algorithm, consisting of quasi-randomly distributed pixels with counts of exactly 4095, which is the upper limit of the CCD's 12-bit analog-to-digital converter. The ring anomaly and measles rarely occur in the region used to compute TII data products, and therefore are believed to have a negligible effect on TII data products, however they continue to be monitored carefully. The recommended method for resolving anomalous behaviors associated with water vapor is to bake the detector at 100 C or more for several hours. This addition of heaters to effect such a bakeout on orbit was considered to be unfeasible during the development phase.

Table 4 summarizes imaging anomalies that can directly affect ion drift measurement performance. All TII full image pairs (H and V) obtained during TII science operations between 9 December 2013 and 28 May 2022 were analyzed. Science operations are identified based on instrument voltages for which MCP input surface voltage is less than − 1000 V, phosphor voltage is greater than 3900 V, and inner dome bias voltage is less than − 50 V. This excludes all TII calibration mode and scrubbing imagery. Occurrence probabilities for each sensor are shown in the table. Upper and lower angel's wings statistics are provided separately. Image analysis was rudimentary. Angel's wings, peripheral, and measles anomalies are identified when pixel counts within fixed detector regions exceed arbitrarily chosen thresholds. The probability of occurrence signifies the ratio of the number of images flagged as having the anomaly to the total number of images analyzed and does not indicate the severity of the anomaly. The bifurcation anomaly is identified by comparing counts of six pixels centered on the image first moment with those three rows above and those three rows below. The classic wing anomaly is identified where the second y moment is greater than 10 pixel^2. The ring anomaly is difficult to identify automatically and has been excluded from the analysis.

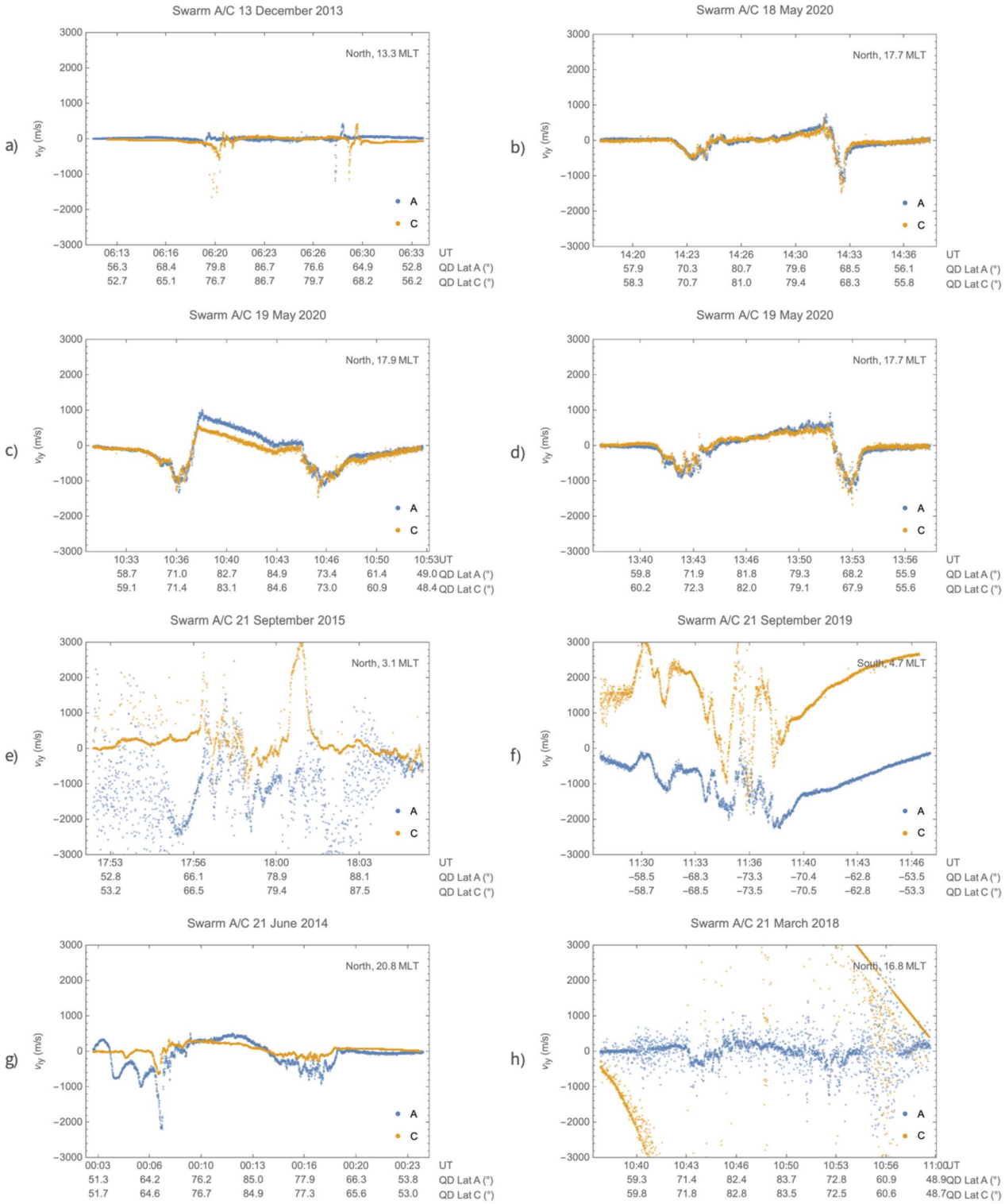

Fig. 11 Examples of realistic and unexpected cross-track horizontal ion drift from Swarm A and C at various epochs of the mission. Each series is from high latitudes, poleward of quasi-dipole latitudes of ±50°. Cross-track horizontal ion drifts (v_{iy}) from the TII cross-track ion drift dataset, version 0302, are shown for Swarm A (blue dots) and C (yellow dots). The hemisphere (north or south) and magnetic local time at the beginning of the interval are shown inset in each plot. See the "Swarm TII flight performance" section for discussion

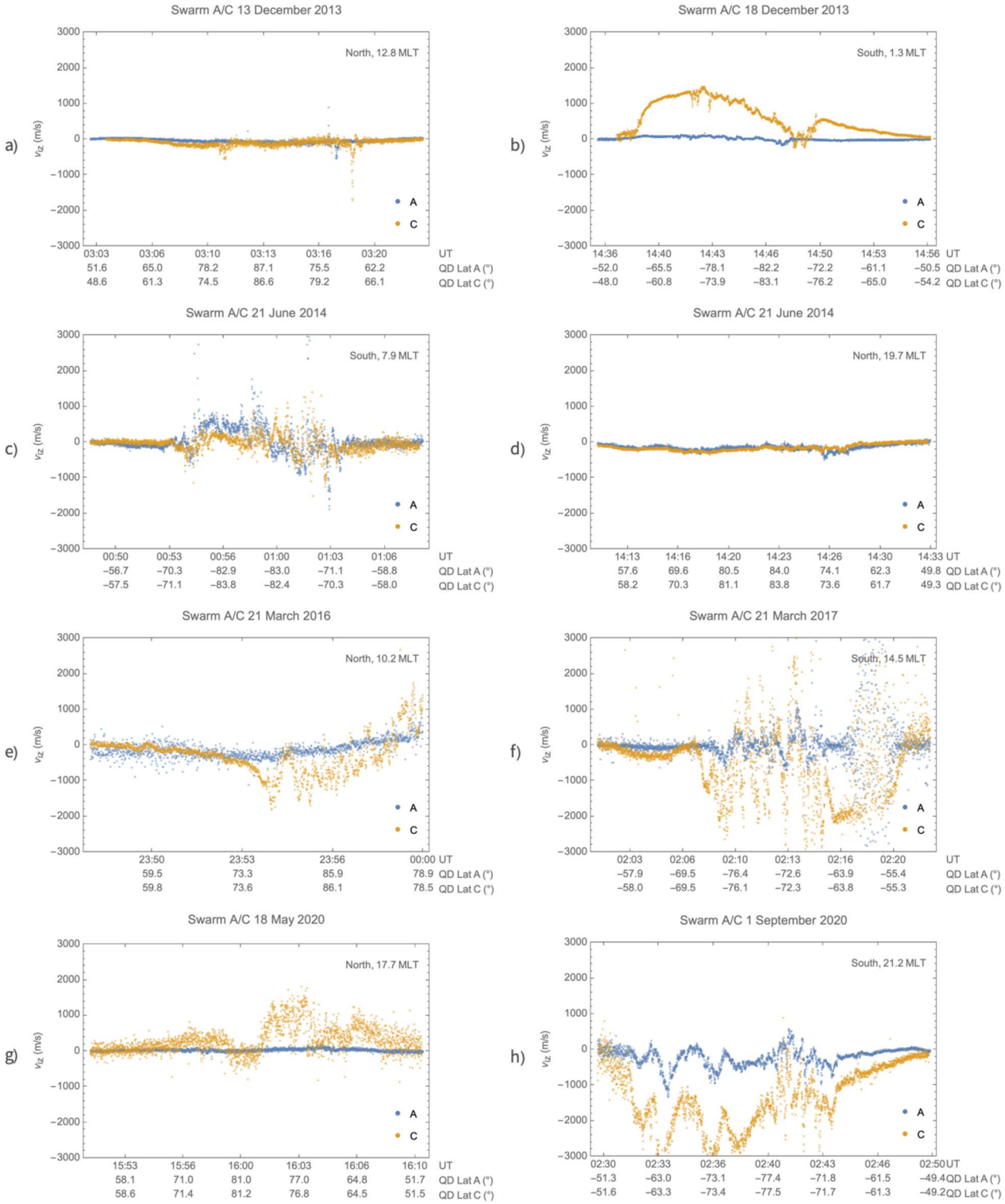

Fig. 12 Examples of realistic and unexpected vertical ion drift from Swarm A and C at various epochs of the mission. Each series is from high latitudes, poleward of quasi-dipole latitudes of ±50°. Cross-track horizontal ion drifts (v_{iy}) from the TII cross-track ion drift dataset, version 0302, are shown for Swarm A (blue dots) and C (yellow dots). The hemisphere (north or south) and magnetic local time at the beginning of the interval are shown inset in each plot. See the "Swarm TII flight performance" section for discussion

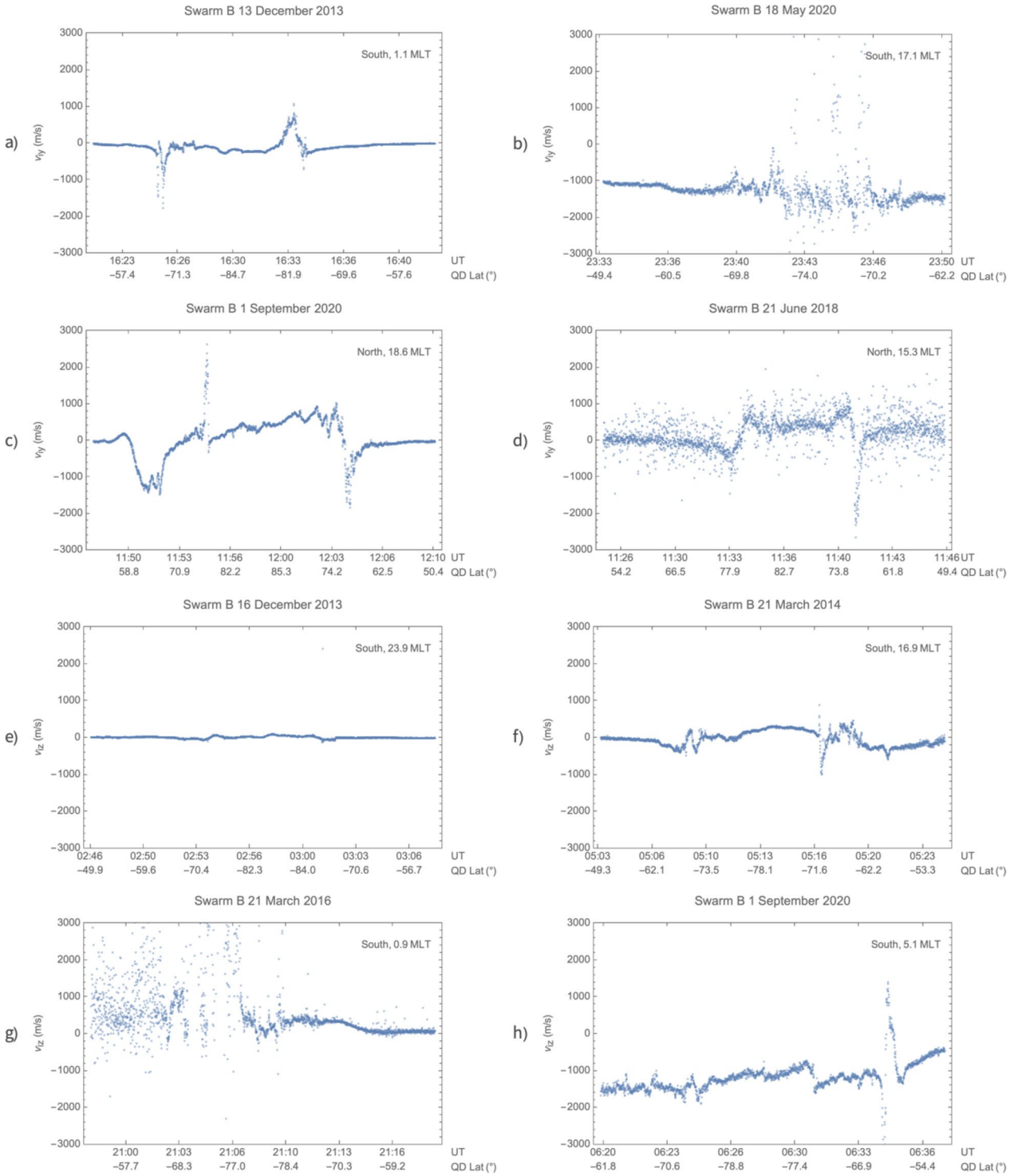

Fig. 13 Examples of realistic and unexpected cross-track horizontal and vertical ion drift from Swarm B at various epochs of the mission

Angel's wings are more prevalent in the upper part of the image than the lower part for all six sensors. On the order of 2% of images have an identifiable bifurcation anomaly. Around 10% of images exhibit the classic wing anomaly. Peripheral anomalies are prevalent in all six sensors. Only the Swarm C H sensor exhibits significant levels of the measles anomaly (0.9%), consistent with a cause arising from within the device or its electronics.

Table 4 does not provide information about the locations of the anomalies, nor their distribution and evolution in time. We plan to apply more sophisticated analysis techniques, such as machine learning, to accurately flag all TII imaging anomalies and further examine their occurrence statistics, causes, and effects on the ion drift and electric field measurements in a future study.

The effects of all detector anomalies on TII imaging are the subject of an ongoing Anomaly Review Board investigation led by ESA and supported by the University of Calgary and industry. This investigation includes an extensive in-flight experimental campaign involving tuning of TII operating points, high-voltage scheduling, satellite maneuvers, a ground-test campaign using a high-intensity ion source, and a review of the sensor engineering design to address known problems, the results of which are planned be the focus of separate paper.

Ion drift velocity

The unexpected prevalence and variety of measurement and imaging anomalies arising both internally (from water vapor) and externally (from satellite–plasma interactions), coupled with noise issues in the satellite potential, proved to be too great a challenge for the automatic processing of ion drifts and temperatures envisioned for the original operational level 1b processor. This necessitated disabling the TII component of the operational processor and instead adopting a simplified approach focusing on the more robust cross-track ion drift, as represented in a reference frame moving with the satellite. The remainder of this paper addresses the measurement performance of the version 0302 TII cross-track ion drift dataset, available in the "Advanced" folder at ESA's Swarm data website (https://swarm-diss.eo.esa.int). The processing and calibration scheme is covered in detail in the dataset release notes (Burchill and Knudsen 2020), available from the same website. Those wishing to use EFI ion drift measurements are encouraged to review that document carefully.

Table 5 TII cross-track ion drift dataset quality (TCT02 version 0302). Shown are the total number of records analyzed, the fraction of total cross-track horizontal (Viy) drifts flagged as good quality, and the fraction of high-latitude drifts flagged as good quality. Data quality is unavailable for Swarm C

Satellite	Swarm A	Swarm B
Total measurements	219,832,253	207,427,058
Good-quality fraction (all)	0.391	0.395
High-latitude records	85,890,573	81,984,328
Good-quality fraction (high-latitude)	0.882	0.894

The TII cross-track ion drift dataset version 0302 provides estimates of cross-track ion drift in a reference frame co-rotating with the Earth, the drifts being derived from lateral displacement of the ion spot as measured by the y first moment, rather than from the deflection of the spot's angular position as was the case in previous versions (e.g., Koustov et al. 2019). The sensitivity of each sensor's variation in y first moment to variations in cross-track ion drift has been calibrated using an in-flight attitude sweep maneuver on each satellite with varying degrees of success. Version 0302 introduces estimates of random velocity errors and a more robust approach to flagging data quality and characterizing the calibration process (Burchill and Knudsen 2020).

Figures 11, 12, and 13 show examples of both realistic and non-geophysical high-latitude cross-track horizontal ion drift at various epochs throughout the mission. These samples give a good indication of the range of data quality in the datasets. The examples are not meant to represent relative occurrence rates. The purpose of these figures is to provide clear examples of the types of measurements obtained by the TIIs to give users an indication of what to watch out for when interpreting the drifts. Most examples are at high latitude as this is where geophysical flows exceeding several hundred m/s are most clearly seen and with obvious relation to auroral zone flow characteristics. The dates are chosen in an ad hoc manner, and the ordering of the panels is not significant. In each panel the Swarm A measurements are shown in blue points, and the Swarm C data are shown in yellow points. We have ignored quality flags in producing Figs. 11 and 12. All plots share a common ordinate range to allow direct comparison of measurement performance at different times of the mission. The hemisphere (north or south) and magnetic local time at the beginning of the interval are indicated. Each series covers high latitudes, i.e., poleward of quasi-dipole latitudes of $\pm 50°$. Residual offsets in cross-track ion drifts are removed by least-squares fitting a linear model to the low-latitude portion of each series on either side of the pole. (e.g., quasi-dipole latitudes from 44° to 50° in the northern hemisphere) as described in Burchill and Knudsen (2020).

Figure 11a shows Birkeland current boundary flows (Archer et al. 2017) from 13 December 2013, shortly following high-voltage commissioning at a time when Swarm A led Swarm C by approximately 57 s in the same orbit. At this time both ion input fluxes and detector gains were highest, and the noise levels were small. The remaining plots show data from after the commissioning period, when Swarm C leads Swarm A by 4 s to 10 s along similar but not identical orbits. Figure 11b–d shows periods of very high correlation in the measurements from the two satellites. It is not known whether the ∼400 m/s

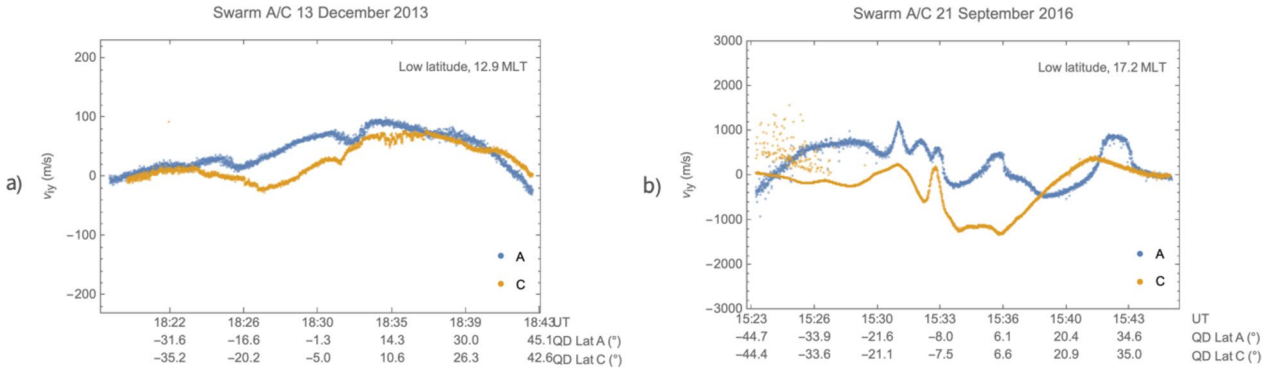

Fig. 14 Examples of unexpected low-latitude cross-track horizontal ion drift from Swarm A and C at two epochs of the mission. Each time series is centered at the magnetic equator

difference over the polar cap in Fig. 11c is an artifact or rather signifies geophysical variation on a 1-min time scale. The remaining examples in Fig. 11 show various cases of poorer measurement performance for one satellite or the other, or, in the case of Fig. 11h, the inability of the processing algorithm to calibrate the flows.

Owing to difficulties in estimating ion drift sensitivities from the in-flight calibration scheme, and also to the typically poorer performance of Swarm C's TIIs, version 0302 data are flagged as usable only for the cross-track horizontal ion drift from Swarm A and B at high latitudes (quasi-dipole magnetic latitudes poleward of ±50°). Due to the typically large flow magnitudes observed at low latitudes the processor excludes low latitude measurements from the flagging. Table 5 provides an overview of the fractions of total cross-track horizontal records of the 2 Hz TII cross-track flow dataset (variable Viy in TCT02 version 0302) that are flagged as having good quality based primarily on having low variability at mid-latitude. There are many periods in the dataset for which Swarm C provides high-quality measurements, and there are also high-quality vertical ion drifts from all satellites; however, the in-flight calibrations have been difficult to interpret, and the drifts are provided as-is to facilitate calibration and validation work within the community. For geophysical investigations, care must be taken to assess data quality. Some examples of vertical ion drifts, again from Swarm A and C, are shown in Fig. 12 for various dates throughout the mission.

Both systematic and random errors vary significantly throughout the mission. Although there is a systematically larger random error for smaller ion input fluxes (i. e., smaller ion densities), as seen in the larger scatter in drifts at lower latitudes on the night-side of each polar pass (e.g., Fig. 12c), sometimes larger random errors are associated with imaging anomalies (like angel's wings, peripheral anomalies, and measles), improper automatic gain control operation, or low input flux for one sensor

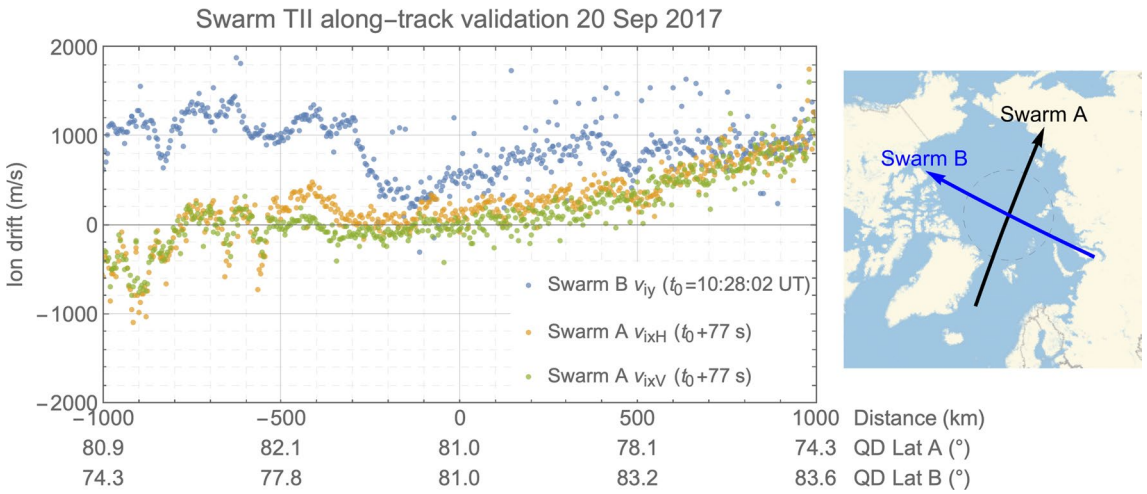

Fig. 15 Comparison of Swarm A along-track drifts with Swarm B cross-track drift during a close conjunction

versus the other. This last case occurred on Swarm C for approximately one year from mid-2019 to mid-2020 when the EFI faceplate voltage, which nominally is set to − 1 V for TII operations, was set to − 3.5 V to support faceplate current measurements (from which a 16 Hz ion density product is produced by IRF). The reason for the lower input flux at the lower faceplate voltage is not well understood, but it is likely associated with deflection of ions by the satellite sheath. The effect is to produce noisier ion drift data, as shown for example in Fig. 12g. The examples of Swarm B cross-track horizontal and vertical ion drift shown in Fig. 13 reveal a similar variety of data quality in terms of geophysical signatures, noise levels, and systematic offsets.

Figure 14 illustrates with two examples the low-latitude cross-track ion drift. While there are cases throughout the mission where the amplitudes of the equatorial and mid-latitude flows are at most 100 m/s (e.g., Fig. 14a), the majority of low-latitude observations show large-amplitude structure of order 1 km/s (e.g., Fig. 14b), often with little correlation between Swarm A and C. Low and middle latitude flows are usually expected to be on the order of one m/s or tens of m/s, associated for example with the equatorial Sq current system and the equatorial electrojet, although some examples of large flow have been reported (e.g., Aggson et al. 1992; Hanson et al. 1997). The flows shown in Fig. 14a appear to show small-scale structures, and Swarm A and C, which fly 57 s apart on almost the same trajectory, show similar large-scale variations. The nature of the anomalously large measurements often observed at low and middle latitudes (in Fig. 14b, for example) is under investigation, and consequently the current version of the TII cross-track ion drift dataset does not flag low-latitude flows for geophysical study.

Along-track ion drifts are provided in the 0302 dataset for reference. Due to the routine presence of spikes and high-frequency noise in the spacecraft potential estimate,

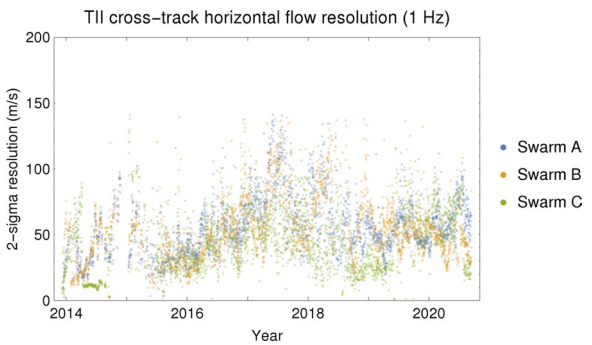

Fig. 16 Daily TII 2σ velocity resolution from the version 0302 cross-track ion flow dataset

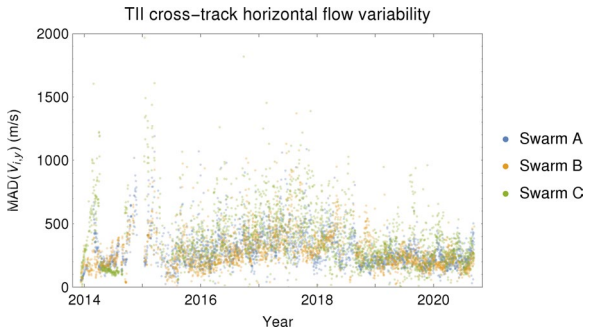

Fig. 17 Daily TII horizontal cross-track ion flow variability from version dataset 0302, estimated from the median absolute deviation of polar cross-track horizontal (v_{iy}) measurements

along-track drifts are converted to velocities directly from the first image moment, and spacecraft potential is not accounted for in the processing. Such data may be directly useful in studies of large, localized flows such as those at high latitude (e.g., the high-latitude convection reversal boundary), but need additional processing to improve the accuracy of along-track drifts and cross-track electric fields.

Although the along-track data are not flagged in the processor as useful for geophysical study, there are nevertheless cases of high-quality along-track flows. One example is shown in Fig. 15. This examines the validity of the Swarm A along-track ion drift with respect to cross-track ion drift measured by Swarm B during a close conjunction of the satellites on 20 September 2017. The satellites traverse the northern polar cap at almost right angles to each other (see the right-hand side of Fig. 15). The panel at left shows the cross-track ion drift from Swarm B and the two estimates of along-track drift from Swarm A versus distance in kilometers along each satellite's trajectory relative to the cross-over point. Negative distances indicate measurements obtained prior the cross-over point. Swarm B reaches the cross-over point at 10:28:02 UT, and Swarm A reaches the same geographic position 77 s later. The ion drifts in Fig. 15 are not instantaneous snapshots, and the flow measured by Swarm B may be substantially different by the time Swarm A reaches the same location. Moreover, the timing is based only on the satellite speed and does not take into account ionospheric convection.

The so-called along-track drifts in the 0302 dataset are derived in a similar manner to the cross-track drifts, that is, they are based on direct conversion of moments to velocities, not taking into account variations in total ion energy. For this analysis we first convert the drifts to obtain kinetic energies as would be directly measured by

the TIIs. This amounts to assuming pure O^+ shifted into the satellite frame by the satellite speed of 7.6 km/s. We correct these energies for the spacecraft potential and faceplate voltage (of − 1.0 V) before converting back to velocity and removing the satellite motion. An energy offset is subtracted for each sensor to ensure the resulting along-track velocity is ∼0 m/s at 50° quasi-dipole latitude.

The dashed circle on the map has a radius of 1000 km to indicate the region of interest under examination in the spatial series on the left-hand side of Fig. 15. Within this circle we have assumed a time-independent ionosphere over the 77 s revisit time. Differences between the along-track and cross-track measurements are estimated from the median of the 11 nearest measurements to the cross-over point in each case. The median velocities at the cross-over point are $v_{iyB} = 573\,\mathrm{m/s}$, $v_{ixHA} = 94\,\mathrm{m/s}$, and $v_{ixVA} = -25\,\mathrm{m/s}$, meaning that the Swarm A horizontal along-track ion drift is within 500 m/s of the Swarm B measurement, and the Swarm A vertical along-track ion drift is within 600 m/s of the Swarm B measurement.

As an assessment of long-term trends in the TII cross-track ion drift measurement resolution, Fig. 16 shows the 2σ v_{iy} velocity resolution, as calculated from the mean absolute deviation of the mid-latitude background flow between quasi-dipole latitudes of 44° and 50° (both northern and southern hemispheres), where ion drifts are expected to have very small magnitudes, on the order of tens of m/s typically. Measurements from all three satellites are shown irrespective of quality flag. The lower bound of the data for each satellite gives an indication of the best attainable velocity resolution, typically of order 10 m/s to 20 m/s (2σ) at 1 Hz for the sunlit portion of each interval. The faceplate bias effect, where the Swarm C TII input fluxes are significantly lower at a faceplate voltage of − 3.5 V versus high fluxes at − 1 V, is seen as a higher noise level from mid-2019 to mid-2020.

A measure of high-latitude cross-track horizontal geophysical variability, again estimated using the median absolute deviation but now for each entire polar pass, is shown in Fig. 17. The noticeably smaller variability for all satellites starting in the latter half of 2018 is coincidental with the transition in inner dome bias voltage from − 60 V to − 100 V, a change which was aimed at bringing the oxygen ion signal onto a less-exposed, and therefore higher-gain, region of each detector. We note that TII MCS simulations reveal that the sensitivity of the sensor to cross-track horizontal drift depends on inner dome bias voltage. The in-flight sensitivity calibrations performed in late 2019 were done for a bias of − 100 V. This calibration has been propagated to the - 60 V operations using the TII MCS. The variability is systematically of order 30% to 50% smaller at − 100 V than at − 60 V, which suggests that the − 60 V calibration needs to be revisited.

Discussion

Our focus since the Swarm launch has been on understanding the unanticipated TII measurement issues and on improving the processing of ion drift, which is generally much less susceptible to imaging artifacts than is ion temperature. Recovery of ion temperature from the TII data is possible (Fig. 9d of Knudsen et al. 2017). An ion temperature estimate based on heat balance between ionospheric electrons (measured by the LP), ions, and thermospheric neutrals (characterized using empirical models) has been developed at the University of Calgary under contract to the Danish Technical University as a project of the Swarm Data, Innovation and Science Cluster consortium (Lomidze et al. 2021). The ion temperature model should aid development and validation of TII ion temperature processing.

Figures 11 through 14 provide typical examples of ungeophysical signatures of the ion drift. Similar behavior will appear also in the electric field. A statistical survey of occurrence rates and locations and times has been initiated, but validation of results is ongoing. We leave this for a future publication involving application of machine learning to flagging spurious signals in the TII data and providing statistical characterization. In the meantime, users are invited to visit "http://efi.phys.ucalgary.ca/SwarmMovies" to review the available TII imagery and to contact the UCalgary EFI team when investigating specific time series of the TII cross-track ion drift measurements.

Precision measurement of the ram component of ion drift velocity from an orbital platform requires precision measurement of satellite floating potential. In principle, satellite floating potential may be estimated by comparing the ram energies of the dominant O^+ species and the typically next most abundant species, H^+, assuming both species approach the satellite with the same ram speed. This has been used extensively with the retarding potential analyzer technique (Hanson and Heelis 1975). It was found in both simulation and experience with the TII images, however, to be difficult to calculate reliably the satellite floating potential with the desired precision and accuracy. On Swarm the satellite floating potential is estimated by two Langmuir probes. Langmuir probe simulations were included in the EES courtesy of IRF. Attempts to assess the estimates of satellite potential have been hindered by large-amplitude noise trains and occasionally by large, apparently systematic errors. According to simulations with the TII MCS, variations in satellite floating potential do not significantly affect cross-track

ion drift estimates, and consequently the cross-track ion drift processor does not use the floating potential measurement. Detailed analysis of the Langmuir probe performance is an ongoing part of Swarm calibration and validation activities, and it is beyond the scope of this paper to comment further.

Particle-in-cell simulations (e.g., Marchand et al. 2010; Rehman et al. 2012, 2013) have been able to provide insight into the effect of the spacecraft sheath on TII performance. Distortions of ion distribution functions arising from the spacecraft sheath and Earth's magnetic field can cause systematic velocity errors exceeding 50 m/s in cases where the plasma density falls below $10^3\,\mathrm{cm}^{-3}$ and ion temperature exceeds 5000 K (Marchand et al. 2010). These conditions are never met with the International Reference Ionosphere model. In practice, ion temperatures exceeding 5000 K (typically occurring in localized regions of the auroral zones; see Shen et al. 2018; Archer et al. 2015) will require expert attention to assess the measurements and their errors. Some variations in apparent ion kinetic energy (e.g., Fig. 6) appear to have causes outside the instrument, as they are seen by both sensors at the same time. The angel's wing anomaly (Fig. 7) appears also to have an outside cause. Further expert study is warranted.

Prior to flight, TII detector gain variations were expected to be corrected to residual errors of less than 5% using in-flight calibrations. TII gain correction maps are routinely updated on timescales from months to about a year. Observed gain depletions, at times as deep as 90%, are corrected, but very likely there are regions on each detector with residual gain variations of 5% or more. There is evidence that gain can vary from one day to the next, and within the first orbit of operation on a given day. The gain appears to be stable on timescales of tens of minutes, that is, the time over which the satellite crosses a polar region. Such variations are accounted for by the polar baseline trend estimation and removal in the TII cross-track ion drift processing (Burchill and Knudsen 2020; Lomidze et al. 2019). As shown in this paper, sometimes the offset correction is erroneous, and attention should be paid to the mid-latitude baseline levels when studying individual cases.

Automation was a central requirement for the design of the TII level 1b processing algorithms. Experience has shown that automated processing is very difficult to achieve in practice, especially for estimating calibration parameters. The switch to a simpler processing algorithm that forgoes taking into account some systematic error sources has allowed us to develop an automatic procedure for reducing the 16-Hz moments to cross-track ion drifts. Algorithms for flagging data quality are currently not a replacement for careful review by an expert.

With regard to end-to-end simulations, orbit-averaged comparisons were used to estimate the measurement uncertainties for each product. The reported total uncertainties are larger than are typically reported for other instruments such as the ICON IVM ion drift meter (Heelis et al. 2017). We note the EFI TII resolution of 5 m/s RMS at an ion density of $10^4\,\mathrm{cm}^{-3}$, which is comparable with the precision of the IVM quoted by Heelis et al. (2017). Furthermore, the simulated TII measurement error estimates apply for measurement range requirements of $\pm 4\,\mathrm{km/s}$ corresponding to large flows at auroral latitudes, a range significantly larger than would be required for low-latitude observations. As we have seen, much of the TII error is attributable to simplification of the transfer functions over this wide range of velocities and temperatures. Theoretical TII measurement errors would be much lower if the required velocity range was in line with the typically much smaller flows observed at low-latitudes, and if the processing could be tuned to a relatively confined region at low latitude, because fewer coefficients would be needed in the transfer functions to characterize the parametric relationship between image properties and plasma parameters, resulting in fewer on-orbit measurements required to calibrate the functions. Any comparison of performance for different measurement techniques must therefore consider such issues.

Accuracy is a characterization of systematic error. Clearly much of the systematic error present in the end-to-end simulations could be reduced using sufficiently high-order transfer functions in the level 1b processing. Such functions need to be validated, either with lab testing or with independent measurements such as those from ionospheric radars.

Aside from providing insight into TII performance, it is hoped that the details presented will be useful for assessing error sources for other satellite-borne ion drift and temperature instruments, and in the design of future instruments. The results reported above capture the key measurement error sources identified both prior to and in flight, and can be used to evaluate the realistically best performance achievable by a TII and its data processor as implemented for the measurement ranges required by the Swarm mission. The error estimates tabulated in Table 2 do not fully reflect actual Swarm TII performance because the EES does not include the effect of several types of abnormal features in the TII images that were unknown prior to launch and which have become the focus of an ongoing investigation and test campaign.

As mentioned, the absorption of water vapor prior to launch, particularly by the TII's phosphor screens, and its effect on detector gain was anticipated prior to launch. It was also anticipated, supported by laboratory testing, that the water would be expelled and normal detector

gain would return through normal operation of the instrument on orbit.

However, this prediction was not borne out, likely due in part to two aspects of the laboratory tests that were not fully representative of on-orbit conditions. Specifically, extensive lab-based attempts to expel water were carried out at ambient temperature in the calibration chambers, typically of the order of 25° C, whereas sensor temperature on orbit is consistently below 10° C. The rate of water expulsion is known to depend exponentially on temperature, with the rate approximately doubling for each 10° C (R. Enck, personal communication). The ability to heat the sensor on orbit would have helped considerably in this regard but was excluded due to considerations of design cost and risk. Secondly, in laboratory tests of water expulsion the TII detectors were operated without the ion focusing electrodes and entrance aperture in place, thus allowing for a more rapid expulsion of water than is possible in the flight configuration.

Phosphor-screen-based detectors have been used previously in space-flight missions, but for photon detection, in which case the detector assembly can be baked and sealed prior to launch. While a phosphor-based particle detector could in principle be evacuated and sealed prior to launch, the seal must eventually be broken and any obstructions in the particle path removed on orbit, adding a challenging and risky element to the design which was considered but rejected during the TII development.

To our knowledge, the TII sensors are the first space-based particle detectors to employ a phosphor screen, with the exception of prototype instruments flown on sounding rockets, and the Suprathermal Electron Imager (SEI) on the CASSIOPE/ePOP satellite launched just two months before Swarm (Knudsen et al. 2015). As with the TII sensors, the SEI also was kept under dry nitrogen purge prior to launch up until the late stages of the launch campaign, when a period of exposure to atmosphere was unavoidable. However, the SEI was operated only 5-10 minutes per day on orbit and did not exhibit signs of trapped water vapor that became evident only after weeks of continuous TII operation on Swarm.

The case studies and statistical results of TII ion drift measurement performance described here and in previous validation studies show that generally very high quality data are routinely obtained from the TIIs, even 8 years into a mission for which the instrumentation was designed to last four years. Nevertheless, care should be taken to assess individual time series for particular scientific studies. The various imaging anomalies curbed the original plan to operate the sensors full time, and it is not always possible to find TII ion drifts of good quality for a particular event study. The time-constant for anomalous artifacts is often relatively long; high-pass filtering has proven effective, for example in studies of Alfvén waves and Poynting flux (Park et al. 2016, 2017; Rodríguez-Zuluaga et al. 2017; Wu et al. 2020; Pakhotin et al. 2020).

We find in retrospect that the EES fails to capture accurately the full range of TII measurement errors. Many errors are associated with outgassing effects internal to, and satellite-environment effects external to, the TII sensors, and which were not appreciated prior to flight and not observed in sounding rocket data. The simulations have proven critical for establishing a quantitative foundation for the interpretation of the flight data, facilitating a focused investigation of likely causes, and providing a basis for future research directions aimed at improving the performance of this satellite-borne thermal ion imaging technique.

Conclusion

We have analyzed the error sources and measurement performance of the thermal ion imaging technique as designed and implemented for the Swarm Earth Explorer mission. Results of an end-to-end simulation of TII performance demonstrate the TII can meet requirements for orbit-averaged ion drift resolution of 10 m/s (2σ) at densities of 10^4 cm^{-3} or greater at the Nyquist frequency of 1 Hz, and orbit-averaged ion drift accuracy of 200 m/s (2σ). Theoretical ion drift resolution at 530 km altitude (early mission for Swarm B) is 7 m/s (2σ) in the north component of the NEC frame, 3 m/s (2σ) in the east component, and 2 m/s (2σ) in the center component. Ion drift measurement accuracy is 60 m/s (2σ) in the north and east components and 13 m/s (2σ) in the center component. Theoretical ion temperature accuracy is established to be better than 10% (2σ) for temperatures up to 10,000 K. Despite substantial variation in minor ion composition with altitude, the difference in overall measurement performance between 300 km and 530 km is small.

The initial level 1b processing and calibration scheme was found to be inadequate in the presence of TII measurement anomalies arising from the likely presence of water vapor in the TII sensors absorbed before launch, anomalous satellite–plasma interactions, and noisy or inaccurate Langmuir probe estimates of satellite floating potential. A simpler processor for calculating only the cross-track ion drift suitably recovers a significant amount of high-quality cross-track horizontal ion drift at high latitudes. High correlations in cross-track horizontal ion drift are routinely observed between the Swarm A and C satellites, which have latitude revisit times of 4 s to 10 s, and separations of order 50 km to 100 km at auroral latitudes. One particular validation case demonstrated that the Swarm A along-track ion drifts agreed to within 500 m/s with the Swarm B cross-track horizontal ion drift when the satellites crossed near a common point

at approximately right angles within 77 s of each other. While along-track ion drift and temperature have not yet been produced on a regular basis, a significant fraction of orbits exhibit promising examples of these parameters. Selection, calibration and flagging of these intervals remains an important area of further work.

Variable offsets in all three components of processed ion drift are found to be especially large at low and mid-latitude and remain unexplained. Unexpected features of the TII ion imagery, so-called imaging anomalies, are variously associated with causes either internal or external to the sensors, and remain the focus of an intensive effort to understand and mitigate them. Key to the ongoing success of this investigation and development of an improved ion drift processor has been the availability of raw ion imagery corresponding to two-dimensional ion energy-angle distributions for assessing causes of measurement anomalies.

Appendix A: TII performance requirements

TII measurement performance requirements as defined by the Swarm Mission Advisory Group are listed here for reference:

> **R-EFI-9** The vector electric field components in the NEC frame shall be determined with a random error better than 10 mV/m (2σ)—5 mV/m (2σ) target—for plasma densities greater than $1 \times 10^{10}\,\mathrm{m}^{-3}$ and for ion temperature between 0.1 eV and 1 eV for signals encompassing all scales from global to 10 km (full wavelength).
> **E-EFI-10** The stability in time of the electric field vector components determination in the NEC frame shall be better than 1 mV/m/month (2σ) for the slow variations.
> **R-EFI-12** The ion temperature shall be determined with an accuracy better than 20% for temperatures between 0.1 eV and 1 eV for densities greater than $1 \times 10^{10}\,\mathrm{m}^{-3}$ and encompassing all scales from global to 200 km (full wavelength) for periods up to 3 months. The ion temperature shall be determined with an accuracy better than 10% for plasma conditions specified by the IRI model.
> **R-EFI-13** The ion drift velocity vector components in the NEC frame shall be determined with a random error better than 200 m/s (2σ)—100 m/s target—encompassing all scales from global to 10 km (full wavelength) for periods up to 3 months, for densities greater than $1 \times 10^{10}\,\mathrm{m}^{-3}$, and for ion temperature between 0.1 eV and 1 eV.
> **R-EFI-41** The electric field measurement resolution shall be better than 0.3 mV/m.

Appendix B: Reference frames

Figure 1 of Knudsen et al. (2017) illustrates the relationship between the TII sensor coordinate systems $(x, y, z)_{\mathrm{TII,H}}$ and $(x, y, z)_{\mathrm{TII,V}}$ and the spacecraft frame coordinate system $(x, y, z)_{\mathrm{SCF}}$. Many Swarm measurements, e.g., magnetic field vectors, are given in a geographic reference frame called NEC, which has its unit vectors pointing in the north, east, and center (vertically down) directions at the position $\vec{r}$ of the satellite. The EFI level 1b ion drift and electric field vectors are similarly defined in the NEC frame (see Appendix A for EFI measurement performance requirements), and this system was used for the error study, which was conducted prior to launch.

Statistical analyses of Swarm high-latitude ion drifts (Lomidze et al. 2019, 2021) confirm that the along-track component of ion drift is of significantly lower quality than the cross-track component. Transforming to the NEC frame consequently results in poorer quality of both northward and eastward ion drift components at high latitudes. Therefore, the current ion drift processor implementation provides measurements only in a satellite-velocity-aligned (SVA) frame, which has its x-component parallel to the satellite velocity, its y-component to the right (for an observer facing in the direction of motion), and its z-component vertically downward. This frame differs from the SCF frame by up to several degrees in each axis of roll, pitch and yaw of the satellite. The co-rotation ion drift associated with rotation of the Earth is also removed.

To transform measurements between the SVA frame and the NEC frame, for example in investigations using a local geographic or geomagnetic frame or in computing the Poynting vector, the following relationships are used. The x-component of a vector in the SVA frame is parallel to the satellite velocity vector $\vec{v} = (v_N, v_E, v_C)$. Its y-component is parallel to the cross-product of the satellite velocity vector with the satellite position vector. The z-component completes the orthonormal triad. Given the satellite velocity in the NEC frame (as provided in the TCT 0302 dataset), with speed $v = \sqrt{v_N^2 + v_E^2 + v_C^2}$, the following expression transforms a vector $\vec{a}$ from its representation in the SVA frame to its representation in the NEC frame:

$$\vec{a}_{\mathrm{NEC}} = R_{\mathrm{NEC}\leftarrow\mathrm{SVA}} \cdot \vec{a}_{\mathrm{SVA}}, \tag{B.1}$$

where the 3×3 direction cosine matrix is given by

$$R_{\mathrm{NEC}\leftarrow\mathrm{SVA}} = \begin{bmatrix} \frac{v_N}{v} & -\frac{v_E}{\sqrt{v_N^2+v_E^2}} & -\frac{v_N v_C}{v\sqrt{v_N^2+v_E^2}} \\ \frac{v_E}{v} & \frac{v_N}{\sqrt{v_N^2+v_E^2}} & -\frac{v_E v_C}{v\sqrt{v_N^2+v_E^2}} \\ \frac{v_C}{v} & 0 & \frac{\sqrt{v_N^2+v_E^2}}{v} \end{bmatrix}. \tag{B.2}$$

Its transpose may be used to carry out the inverse transformation.

Appendix C: Instrument simulator image model

To simulate hundreds of thousands of TII images in a reasonable time the EES uses a polar Gaussian model

$$f(r,\phi) = A_0 \exp\left[-\frac{(r-\overline{r})^2}{2\sigma_r^2} - \frac{(\phi-\overline{\phi})^2}{2\sigma_\phi^2}\right], \quad \text{(C.1)}$$

where $\overline{r}$, σ_r, $\overline{\phi}$ and σ_ϕ represent the ion spot peak position and width determined from the TII MCS image as

$$z_0 = \sum_{i=0}^{63}\sum_{j=0}^{63} C_{ij}, \quad \text{(C.2)}$$

$$\overline{r} = \frac{1}{z_0}\sum_{i=0}^{63}\sum_{j=0}^{63} C_{ij}\sqrt{(i-31.5)^2+(j-31.5)^2}, \quad \text{(C.3)}$$

$$\sigma_r^2 = \frac{1}{z_0}\sum_{i=0}^{63}\sum_{j=0}^{63} C_{ij}\left(\sqrt{(i-31.5)^2+(j-31.5)^2}-\overline{r}\right)^2, \quad \text{(C.4)}$$

$$\overline{\phi} = \frac{1}{z_0}\sum_{i=0}^{63}\sum_{j=0}^{63} C_{ij}\tan^{-1}\left[\frac{j-31.5}{i-31.5}\right], \quad \text{(C.5)}$$

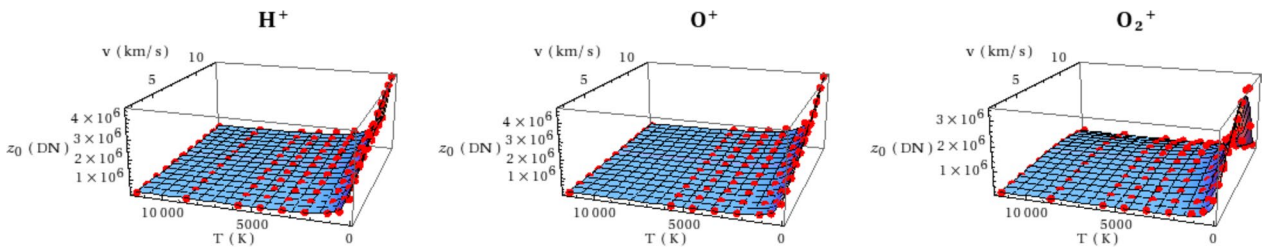

Fig. 18 Least-squares fits (blue surfaces) of EES Gaussian image model parameter z_0 (Equation C.9) to the values determined from TII MCS (red points) as a function of ion ram speed and ion temperature. TII MCS simulations were carried out for three ion species spanning the masses of the IRI model ion composition

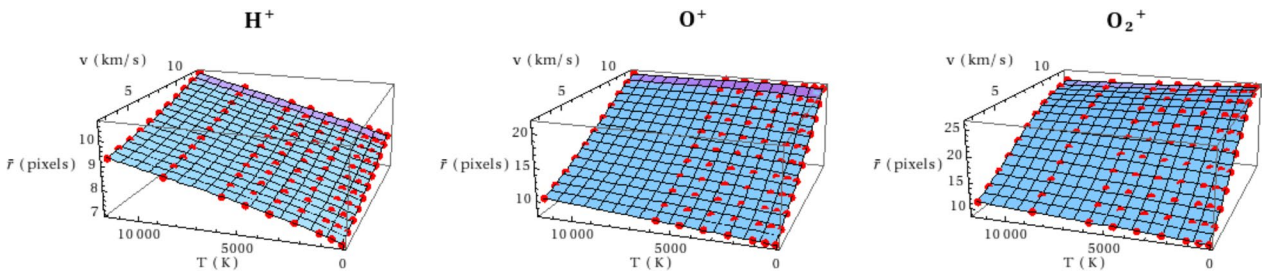

Fig. 19 Least-squares fits (blue surfaces) of EES Gaussian image model parameter $\overline{r}$ (Equation C.10) to the values determined from TII MCS (red points) as a function of ion ram speed and ion temperature for the three ion species simulated

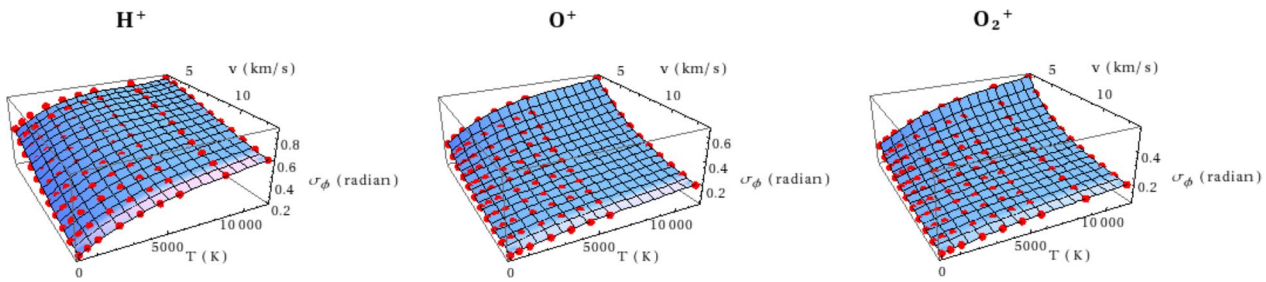

Fig. 20 Least-squares fits (blue surfaces) of EES Gaussian image model parameter σ_ϕ (Equation C.12) to the values determined from TII MCS (red points) as a function of ion ram speed and ion temperature for the three ion species simulated

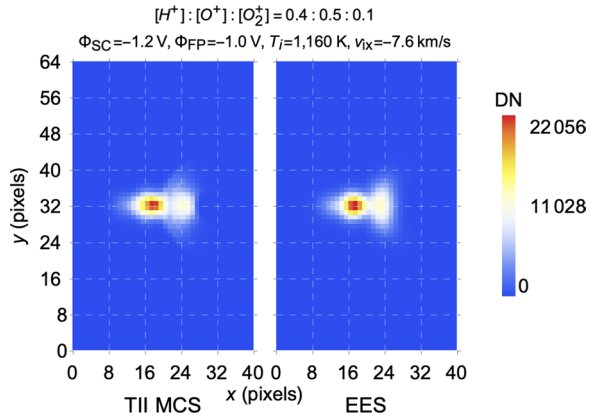

Fig. 21 TII MCS (left) and EES (right) model images for a 1160 K mixed ion population rammed at 7.6 km/s consisting of H^+, O^+ and O^+_2 in relative concentrations of 0.4, 0.5 and 0.1, respectively. A satellite floating potential of - 1.2 V was simulated with a faceplate voltage of - 1.0 V

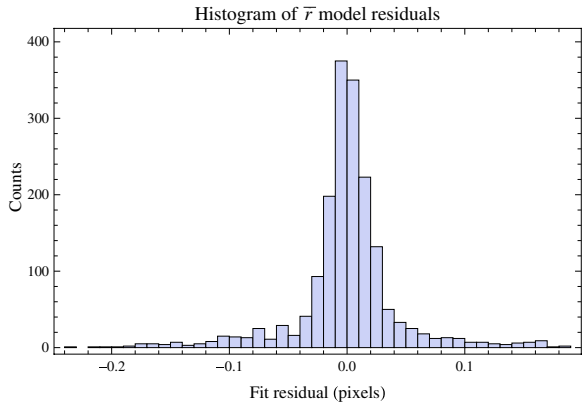

Fig. 22 Fit residuals of $\bar{r}$. The standard deviation 0.044 pixels corresponds to 32 m/s

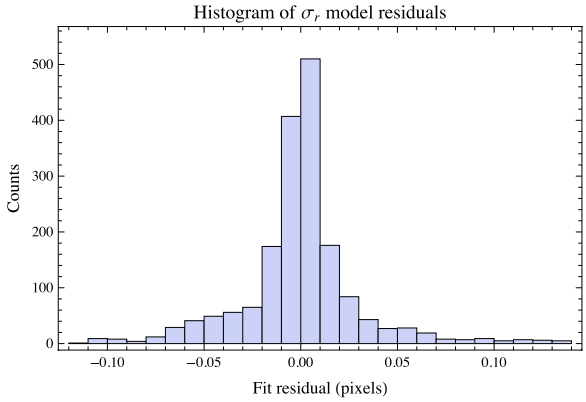

Fig. 23 Fit residuals of σ_r, with standard deviation 0.030 pixels (120 K)

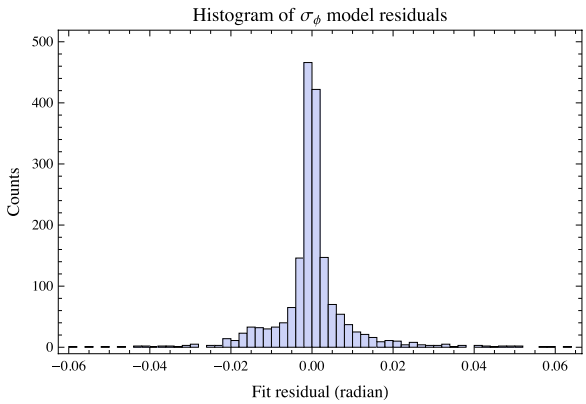

Fig. 24 Fit residuals of σ_ϕ, with standard deviation 0.0097 radian (300 K)

$$\sigma_\phi^2 = \frac{1}{z_0}\sum_{i=0}^{63}\sum_{j=0}^{63} C_{ij}\left(\tan^{-1}\left[\frac{j-31.5}{i-31.5}\right] - \overline{\phi}\right)^2, \quad \text{(C.6)}$$

where i and j are the indices of the image pixel having counts C_{ij}. The spot maximum is given by

$$A_0 = \frac{z_0}{z_{0,\text{Gaussian}}}\frac{t_{\text{int}}}{0.060\text{s}}\frac{n_i}{10^4\text{cm}^{-3}}, \quad \text{(C.7)}$$

where $z_{0,\text{Gaussian}}$is the zeroth moment of the model image when normalized to a peak value of 1, $t_{\text{int}}$is the CCD integration period, and $n_i$is the plasma density.

In the EES the spot polar angle $\overline{\phi}$ is calculated directly from the desired bulk flow velocity in TII sensor coordinates as

$$\overline{\phi} = \tan^{-1}\left[\frac{v_{y,TII}}{v_{x,TII}}\right]. \quad \text{(C.8)}$$

The remaining EES parameters are obtained from multi-dimensional polynomial transfer functions:

$$z_0(E,T,\Phi,m) = \sum_{i=0}^{2}\sum_{j=0}^{2}\sum_{k=0}^{1}\sum_{l=0}^{2} a_{z,ijkl}E^iT^{-j}\Phi^k m^l, \quad \text{(C.9)}$$

$$\bar{r}(E,T,\Phi,m) = \sum_{i=0}^{4}\sum_{j=0}^{3}\sum_{k=0}^{2}\sum_{l=0}^{2} a_{r,ijkl}E^iT^j\Phi^k m^l, \quad \text{(C.10)}$$

$$\sigma_r(E,T,\Phi,m) = \sum_{i=0}^{3}\sum_{j=0}^{3}\sum_{k=0}^{2}\sum_{l=0}^{2} a_{\sigma_r,ijkl}E^iT^j\Phi^k m^l, \quad \text{(C.11)}$$

$$\sigma_\phi(E,T,\Phi,m) = \sum_{i=0}^{3}\sum_{j=0}^{3}\sum_{k=0}^{2}\sum_{l=0}^{2} a_{\sigma_\phi,ijkl} E^i T^j \Phi^k m^l, \tag{C.12}$$

where E, T, and Φ are the ion ram kinetic energy at the entrance aperture, the isotropic ion temperature, and the electric potential difference between the aperture and the plasma, each normalized to the potential difference of the analyzer domes $|\Delta V|$. The plasma density in cm^{-3} is represented by n_i for an ion species with atomic mass number m. The surface fit parameters $a_{X,ijkl}$ are obtained from least-squares fits to the TII MCS image moments spanning the plasma parameter space. Figure 18 shows the parametric dependence of the total signal z_0 on ion ram speed (from 2.6 km/s to 12.6 km/s) and ion temperature (from 116 K to 11600 K, or 0.01 eV to 1 eV) for the three ion species spanning the IRI composition model masses simulated in this study. Red dots indicate TII MCS simulation results. Blue surfaces are least-squares fits of the model to the simulation points. There is a rapid drop in signal with increasing temperature up to several thousand K. For H^+ and O^+ there is a roughly linear dependence of the total signal on ion ram speed, in contrast with the molecular oxygen case, which peaks near the nominal satellite speed. Any dependence of these parameters on the ion flow angle $\bar{\phi}$ has been ignored in this study.

The mean radial coordinate $\bar{r}$ varies with ion ram speed as expected (Fig. 19), and shows a small variation with temperature. The angular width of the model ion spot is captured by σ_ϕ (Fig. 20). There is a strong dependence of the spot width on both ram speed and ion temperature over the parameter space. Figure 21 illustrates a TII MCS image (at left) and its corresponding EES approximation (at right). TII MCS simulations corresponding to an ion temperature of 1160 K (0.1 eV), a ram speed of 7.6 km/s, and a sensor-to-plasma potential difference of 2.2 V are combined for each of the ion species H^+, O^+ and O_2^+ in relative concentrations of 40%, 50%, and 10%, respectively. The EES captures salient features of the TII MCS imagery well for images consisting of multiple ion species.

To assess the adequacy of the EES image models for this study, histograms of fit residuals for the models shown Figs. 19, 20 are shown in Figs. 22, 23, 24. The residuals include all simulation points over all ion species. In Fig. 22 the standard deviation of $\bar{r}$ fit residuals is 0.044 pixels, which corresponds to a 32 m/s standard deviation in ram speed. Figure 23 summarizes the fit residuals for the image model radial width σ_r (which varies predominantly with ion temperature), with a standard deviation corresponding to 120 K. Figure 24 summarizes the fits for the image model azimuthal width σ_ϕ (which also varies mainly with ion temperature), having a standard deviation equivalent to about 300 K. For this study the EES image model captures the TII MCS model imagery with enough fidelity over the large parameter space to justify the gain in speed over the loss of accuracy compared to the TII MCS model.

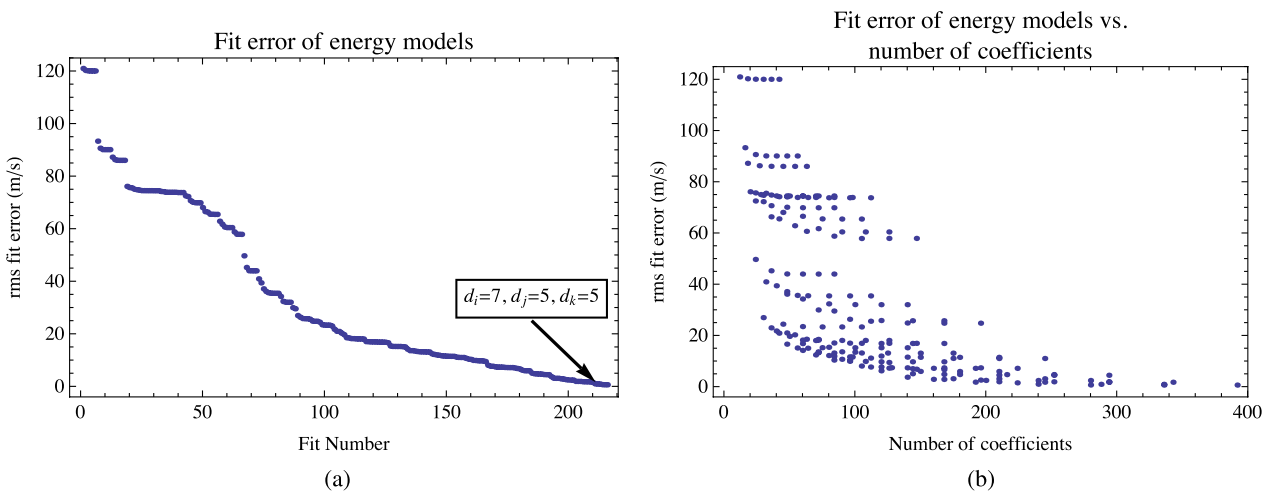

Fig. 25 RMS fit error for the level 1b energy transfer function for models with degree up to 7 in $\bar{r}$, 5 in y_2, and 5 in Φ: (a) in order of decreasing rms error, and (b) in order of the number of coefficients in each fit

Appendix D: Level 1b TII transfer functions

The EES transfer functions of the previous section demonstrate the strong relationship between image moments and the ion drift and temperature. Inverting this relationship to estimate ion drift and temperature from image properties is the role of the level 1b processor (Knudsen et al. 2017). This is accomplished using level 1b TII transfer functions:

$$E(\bar{r}, y_2, \Phi) = \sum_{i=0}^{d_{E,i}} \sum_{j=0}^{d_{E,j}} \sum_{k=0}^{d_{E,k}} a_{E,ijk} \bar{r}^i y_2^j \Phi^k |\Delta V|, \quad \text{(D.1)}$$

$$T_x(\sigma_x, \bar{r}, \Phi) = \sum_{i=0}^{d_{T_x,i}} \sum_{j=0}^{d_{T_x,j}} \sum_{k=0}^{d_{T_x,k}} a_{T_x,ijk} \sigma_x^{2i} \bar{r}^j \Phi^k |\Delta V|, \quad \text{(D.2)}$$

$$T_y(y_2, \bar{r}, \Phi) = \sum_{i=0}^{d_{T_y,i}} \sum_{j=0}^{d_{T_y,j}} \sum_{k=0}^{d_{T_y,k}} a_{T_y,ijk} y_2^i \bar{r}^j \Phi^k |, \Delta V| \quad \text{(D.3)}$$

where the temperature is estimated in orthogonal directions within the planar field of view of each TII sensor.

Table 6 Polynomial degrees for high-order and low-order TII level 1b transfer functions

Parameter	High-order model	Low-order model
$d_{E,i}$	7	4
$d_{E,j}$	5	3
$d_{E,k}$	5	2
$d_{T_x,i}$	7	4
$d_{T_x,j}$	6	2
$d_{T_x,k}$	3	2
$d_{T_y,i}$	6	3
$d_{T_y,j}$	6	3
$d_{T_y,k}$	4	2

The polynomial degree for the model parameter of power i appears as the upper limit of the corresponding summation. For example, the sum over i in the energy transfer function (with factor $\bar{r}^i$) goes up to degree d_{E_i}. Different degrees are used for different models as described below. It is assumed for this study that the transfer functions do not vary with plasma density or flow angle. The peak position $\bar{r}$ is given by

$$\bar{r} = \sqrt{(\bar{x} - x_0)^2 + (\bar{y} - y_0)^2}, \quad \text{(D.4)}$$

where x_0 and y_0 are the coordinates of the TII's symmetry axis in the detector plane. The x-component of the position of the O^+ peak, along with an estimate for its width σ_x , are obtained from a least-squares fit of the Gaussian model

$$N_i = A \exp\left[-\frac{(i - 31.5 - \bar{x})^2}{2\sigma_x^2}\right] \quad \text{(D.5)}$$

to the measured image column sums defined by

$$N_i = \sum_{j=0}^{63} C_{ij}. \quad \text{(D.6)}$$

The y-component of the position of the ion peak $\bar{y}$ is estimated from a linear fit to the 1st moments $\bar{y}_i$ of the eight consecutive brightest columns M calculated onboard the EFI, the fit being evaluated at $\bar{x}$. For T_y, y_2 is estimated onboard using

$$y_2 = \frac{1}{z_0} \sum_{i \in M} \sum_{j=0}^{63} C_{ij} (j - \bar{y}_i)^2. \quad \text{(D.7)}$$

Details and examples of the onboard processing are provided by Knudsen et al. (2017).

Calibration of these level 1b TII transfer functions entails least-squares fitting equations D.1–D.3, where the image parameters are provided by the TIIs and the

Table 7 TII-related data products and processing status

Product	Status
Cross-track horizontal ion drift	TII cross-track drift dataset, version 0302 (see Lomidze et al. 2019)
Cross-track vertical ion drift	TII cross-track drift dataset, version 0302 (not validated statistically)
Proxies for along-track ion drift (H and V sensors)	TII cross-track drift dataset, version 0302 (not validated statistically)
Electric field (SVA frame)	TII cross-track drift dataset, version 0302 (two vector time series are provided using along-track drift from the H and V sensors separately)
Electric field (NEC frame)	Not processed
Ion drift (NEC frame)	Not processed
Ion temperature	Not processed
Ion temperature (SITE)	Swarm Ion Temperature Estimate (Lomidze et al. 2021)

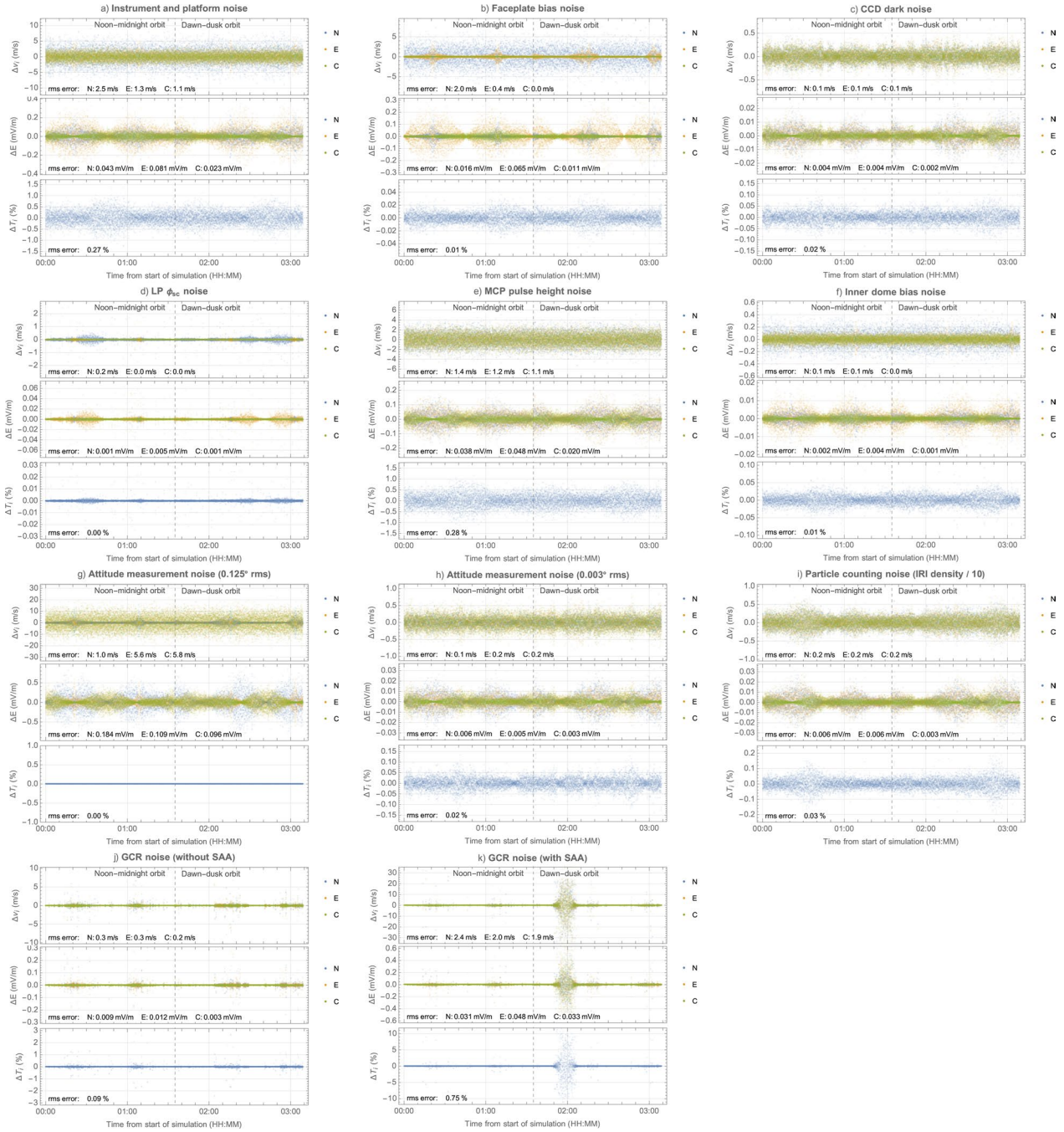

Fig. 26 Time series for random error sources estimated using the EES. For each error source, the plot shows errors in ion velocity (top panel), electric field (middle panel) and ion temperature (bottom panel). The dashed lines mark the artificial transition from a noon–midnight orbit to a dawn–dusk orbit. Data have been downsampled by averaging to the Nyquist frequency of 1 Hz

known ion drift energy and temperatures are measured independently (with an incoherent scatter radar, for example). For such a scheme to be effective, the number of data points must greatly exceed the number of model coefficients and the dataset must span the desired measurement ranges. Over the Swarm mission the number of calibration conjunctions may be in the dozens to hundreds (e.g., Lomidze et al. 2019), so the level 1b transfer functions models are limited to those with perhaps a dozen coefficients. For the purpose of characterizing TII errors associated with using a limited number of transfer function coefficients, a high-order baseline model

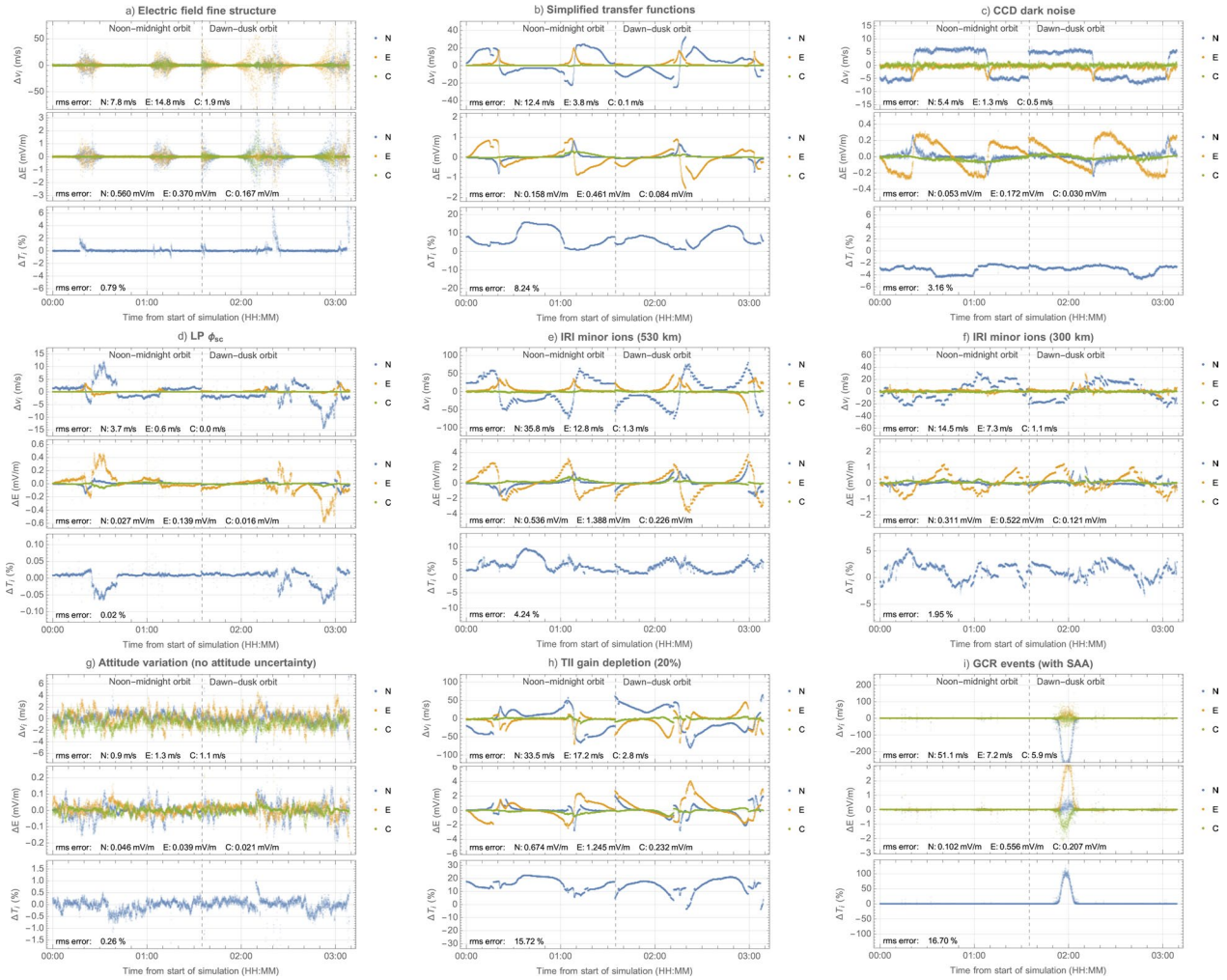

Fig. 27 Time series for systematic error sources estimated using the EES. Plotted in the same format as Fig. 26

is established for which the residual errors are negligible. To illustrate, fits to Equation D.1 were obtained for combinations of degrees in the ranges $2 \leq d_{E,i} \leq 7$, $1 \leq d_{E,j} \leq 6$, and $1 \leq d_{E,k} \leq 6$. Figure 25 demonstrates the nature of the trade-off between number of model coefficients and fit errors. The model of degree (7,5,5) has a fit error of less than 1 m/s. A similar analysis (not shown) was performed for each temperature model. The polynomial degrees in Table 6 summarize the degrees for a reference (high-order) model and a feasible (low-order) model used for assessing transfer-function related measurement errors. Ion drift speed calculated from the high-order energy transfer function model results in a RMS fit error of 0.9 m/s over the measurement range 2.6 km/s to 12.6 km/s. The high-order x and y temperature models have rms errors of 1.2% and 0.4% over the measurement range 116 K to 11600 K (0.01 eV to 1 eV).

Appendix E. Scientific data products

Table 7 lists the current status of various TII-related data products. Although not based on TII measurements, the Swarm Ion Temperature Estimate (SITE) data product (Lomidze et al. 2021) fills a key gap in the original EFI TII products.

Appendix F. EES error source time series

Figures 26 and 27 illustrate the nature of the individual random and systematic noise sources studied with the EES. Each subfigure corresponds an entry in Table 2 and displays the differences between EES outputs and inputs at 1 Hz for ion drift (top panel in each subfigure), electric field (middle panel) and ion temperature (bottom panel). Ion drift and electric field differences are given

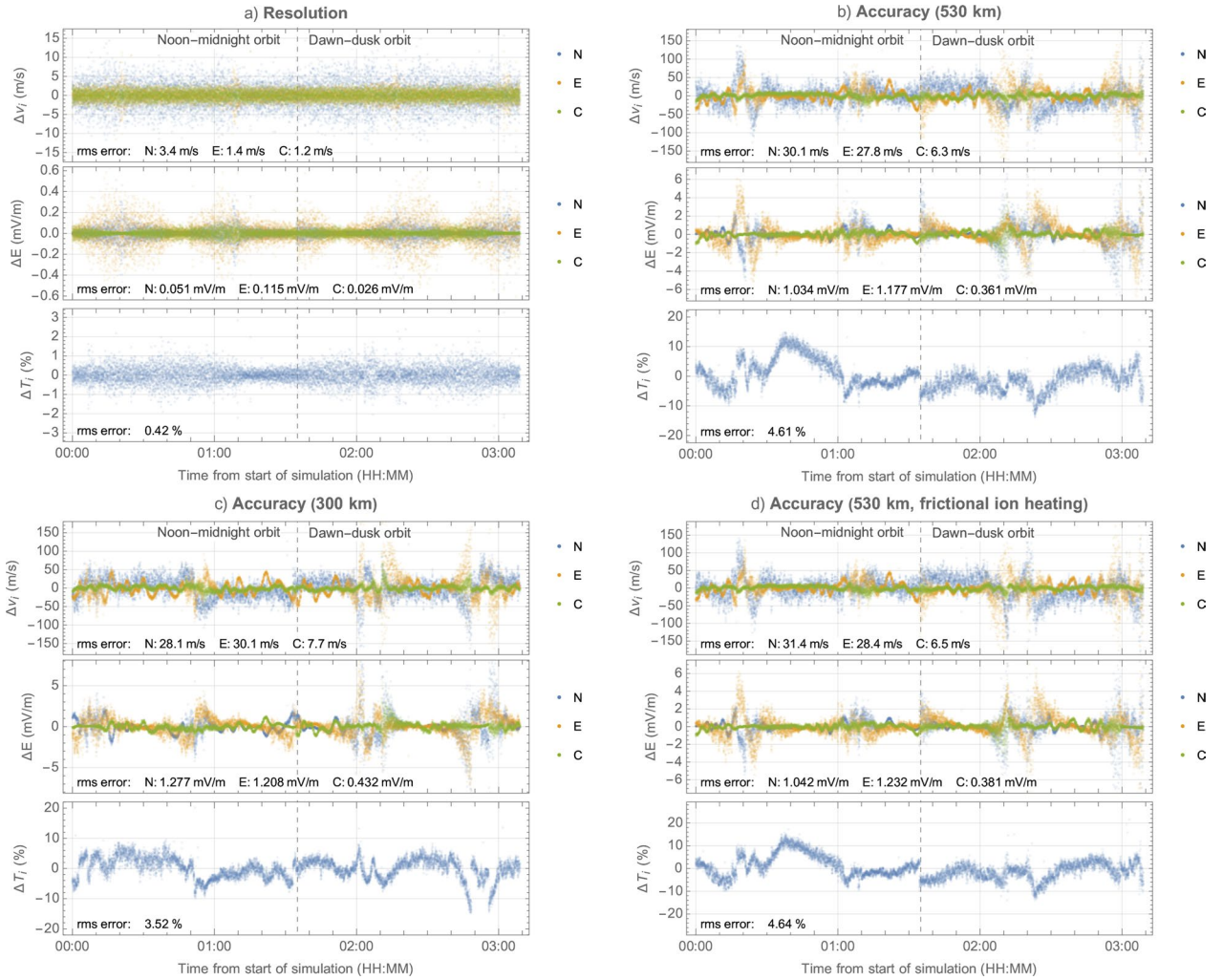

Fig. 28 Time series for total measurement error estimated using the EES, plotted in the same format as Fig. 26: **a** resolution; **b** accuracy at 530 km altitude; **c** accuracy at 300 km altitude; **d** accuracy at 530 km altitude with ion frictional heating at high latitude

with physical units, and ion temperature differences are shown as a percentage relative to the EES input temperature. Errors are provided for all components of the NEC frame for the vector quantities. The time series are unfiltered. RMS differences are calculated as described in the "Methods" section and are summarized in Table 2.

Figure 28 illustrates the differences from which the instrument resolution (Fig. 28a) and accuracy (Fig. 28b to 28d) are estimated. Resolution is estimated with all error sources enabled, both random and systematic, except electric field fine structure and SAA GCRs, for the case of IRI plasma composition, density and temperature at 530 km altitude. Accuracy is estimated with the inclusion of E-field fine structure, and without subtracting random errors, for the nominal start-of-mission Swarm B altitude of 530 km (Fig. 28b) and nominal near-end-of-mission Swarm A and C altitude of 300 km (Fig. 28c). Fig. 28d illustrates accuracy for a simulation incorporating an ad hoc ion frictional heating model to characterize TII performance at temperatures up to the 11,600 K (1.0 eV) measurement requirement.

Abbreviations

AGC	Automatic gain control
CCD	Charge-coupled device
DN	Digital number
EES	End-to-end instrument simulator
EFI	Electric field instrument
ESA	European Space Agency
ESRIN	European Space Research Institute
ESTEC	European Space Research and Technology Centre

FP	EFI faceplate
GCR	Galactic cosmic ray
IDM	Ion drift meter
IRF	The Swedish Institute of Space Physics
IRI	International Reference Ionosphere
ISP	Instrument source packet
IVM	Ion velocity meter
LEP	Low-energy plasma
LP	Langmuir probe
MCP	Microchannel plate
MCS	Monte Carlo simulator
NEC	North, east, center reference system
RMS	Root-mean-square
RPA	Retarding potential analyzer
SAA	South-Atlantic Anomaly
SAIL	University of Calgary Space and Atmospheric Instrumentation Laboratory
SEI	Suprathermal electron imager
SCF	Spacecraft frame
SVA	Satellite-velocity-aligned frame
TII	Thermal Ion Imager
UT	Universal time
UV	Ultraviolet

Acknowledgements
The authors thank Alexei Kouznetsov for invaluable support in curating TII data for daily monitoring and data processing, and for discussions about TII data quality. The authors gratefully acknowledge Richard Enck of Torr Scientific Ltd. for advice about maintaining and improving the TII imaging performance and helping to explain (and name) various imaging anomalies. This study has benefited from guidance and feedback of many people from the European Space Research and Technology Centre (ESTEC), the European Space Research Institute, the European Space Operations Centre, Honeywell (COM DEV), and IRF. IRF contributed to the EFI end-to-end simulator development with respect to Langmuir probe simulation and processing. The authors appreciate the community engagement on TII data quality at the annual ESA Swarm Data Quality Workshop meetings.

Author contributions
JKB developed the TII component of the end-to-end instrument simulator, developed the TII MCS, assisted with lab experiments, analyzed the Swarm data, prepared the figures, and wrote the paper. DJK developed and led the TII measurement performance study, carried out lab experiments, contributed to the interpretation of the results, and assisted in the writing of the paper. Both authors read and approved the final manuscript.

Funding
This study was supported with funding from the Canadian Space Agency and the European Space Agency.

Availability of data and materials
The Swarm level 1b datasets analyzed during the current study are available in the ESA Swarm repository, http://swarm-diss.eo.esa.int. Up-to-date daily movies of TII full imagery can be accessed at http://efi.phys.ucalgary.ca/SwarmMovies. Other data are available from the corresponding author on reasonable request.

Declarations

Competing interests
The authors declare that they have no competing interests.

Author details
[1]Department of Physics and Astronomy, University of Calgary, Calgary, AB, Canada.

Received: 20 August 2022 Accepted: 6 November 2022
Published: 9 December 2022

References

Aggson TL, Burke WJ, Maynard NC, Hanson WB, Anderson PC, Slavin JA, Hoegy WR, Saba JL (1992) Equatorial bubbles updrafting at supersonic speeds. J Geophys Res Space Physics 97:8581–8590
Archer WE, Knudsen DJ, Burchill JK, Patrick MR, St-Maurice J (2015) Anisotropic core ion temperatures associated with strong zonal flows and upflows. Geophys Res Lett 42:981–986
Archer WE, Knudsen DJ, Burchill JK, Jackel BJ, Donovan EF, Connors MG, Juusola L (2017) Birkeland current boundary flows. J Geophys Res 122:4617–4627
Bilitza D, Reinisch BW (2008) International reference ionosphere 2007: improvements and new parameters. Adv Space Res 42:599–609. https://doi.org/10.1016/j.asr.2007.07.048
Burchill J, Clemmons J, Knudsen D, Larsen M, Nicolls M, Pfaff R, Rowland D, Sangalli L (2012) High-latitude E region ionosphere-thermosphere coupling: a comparative study using in situ and incoherent scatter radar observations. J Geophys Res Space Phys 1978–2012:117
Burchill JK, Knudsen DJ (2020) EFI TII cross-track flow data release notes, Technical Report, University of Calgary
Burchill JK, Knudsen DJ, Bock BJJ, Pfaff RF, Wallis DD, Clemmons JH, Bounds SR, Stenbaek-Nielsen H (2004) Core ion interactions with BB ELF, lower hybrid, and Alfvén waves in the high-latitude topside ionosphere. J Geophys Res (Space Phys) 109:1219. https://doi.org/10.1029/2003JA010073
Burchill JK, Knudsen DJ, Clemmons JH, Oksavik K, Pfaff RF, Steigies CT, Yau AW, Yeoman TK (2010) Thermal ion upflow in the cusp ionosphere and its dependence on soft electron energy flux. J Geophys Res. https://doi.org/10.1029/2010JA015006
Chang T, Crew GB, Hershkowitz N, Jasperse JR, Retterer JM, Winningham JD (1986) Transverse acceleration of oxygen ions by electromagnetic ion cyclotron resonance with broadband left-hand-polarized waves. Geophys Res Lett 13:636
Fiori RAD, Koustov AV, Boteler DH, Knudsen DJ, Burchill JK (2016) Calibration and assessment of Swarm ion drift measurements using a comparison with a statistical convection model, Earth. Plan Space 68:1–17
Friis-Christensen E, Lühr H, Knudsen D, Haagmans R (2008) Swarm-an earth observation mission investigating geospace. Adv Space Res 41:210–216
Galassi M, Davies J, Theiler J, Gough B, Jungman G, Alken P, Booth M, Rossi F (2009) GNU scientific library reference manual, 3rd Edn. ISBN 0954612078, Network Theory Ltd
Hanson W, Coley W, Heelis R, Urquhart A (1997) Fast equatorial bubbles. J Geophys Res Space Phys 102:2039–2045
Hanson WB, Heelis R (1975) Techniques for measuring bulk gas-motions from satellites. Space Sci Instrum 1:493–524
Heelis R, Stoneback R, Perdue M, Depew M, Morgan W, Mankey M, Lippincott C, Harmon L, Holt B (2017) Ion velocity measurements for the ionospheric connections explorer. Space Sci Rev 212:615–629
Juusola L, Archer WE, Kauristie K, Burchill JK, Vanhamäki H, Aikio AT (2016) Ionospheric conductances and currents of a morning sector auroral arc from Swarm-A electric and magnetic field measurements. Geophys Res Lett 43:11–519
Knudsen DJ, Burchill JK, Berg K, Cameron T, Enno GA, Marcellus CG, King EP, Wevers I, King RA (2003) A low-energy charged particle distribution imager with a compact sensor for space applications. Rev Sci Instrum 74:202–211. https://doi.org/10.1063/1.1525869
Knudsen DJ, Burchill JK, Cameron TG, Enno GA, Howarth A, Yau AW (2015) The CASSIOPE/e-POP suprathermal electron imager (SEI). Space Sci Rev 189:65–78
Knudsen DJ, Burchill JK, Buchert SC, Eriksson AI, Gill R, Wahlund J, Åhlen L, Smith M, Moffat B (2017) Thermal ion imagers and Langmuir probes in the Swarm electric field instruments. J Geophys Res 122:2655–2673
Koustov AV, Lavoie DB, Kouznetsov AF, Burchill JK, Knudsen DJ, Fiori RAD (2019) A comparison of cross-track ion drift measured by the satellites

and plasma convection measured by SuperDARN. J Geophys Res 124:4710–4724. https://doi.org/10.1029/2018JA026245
Lomidze L, Burchill JK, Knudsen DJ, Kouznetsov A, Weimer DR (2019) Validity study of the Swarm horizontal cross-track ion drift velocities in the high-latitude ionosphere. Earth Space Sci 6:411–432
Lomidze L, Burchill JK, Knudsen DJ, Huba JD (2021) Estimation of ion temperature in the upper ionosphere along the Swarm satellite orbits. Earth Space Sci 8(11): e2021EA001925
Lundin R, Haerendel G, Grahn S (1998) Introduction to special section: the Freja Mission. J Geophys Res 103:4119
Marchand R, Burchill JK, Knudsen DJ (2010) Modelling electrostatic sheath effects on Swarm electric field instrument measurements. Space Sci Rev 156:73–87
Miles D, Mann IR, Pakhotin I, Burchill JK, Howarth AD, Knudsen DJ, Lysak RL, Wallis D, Cogger L, Yau A (2018) Alfvénic dynamics and fine structuring of discrete auroral arcs: Swarm and e-POP observations. Geophys Res Lett 45:545–555
Olsen N, Friis-Christensen E, Hulot G, Korte M, Kuvshinov A, Lesur V, Lühr H, Macmillan S, Mandea M, Maus S et al (2004) Swarm end-to-end mission performance simulator study, ESA contract No 17263/03/NL/CB, DSRI Report 1/2004. Danish Space Research Institute, Copenhagen
Pakhotin I, Mann I, Knudsen DJ, Lysak R, Burchill JK (2020) Diagnosing the role of Alfvén waves in global field-aligned current system dynamics during southward IMF: swarm observations. J Geophys Res 125:e2019JA027Ã‚Â 277
Pakhotin IP, Mann IR, Kai X, Burchill JK, Knudsen DJ (2021) Northern preference for terrestrial electromagnetic energy input from space weather. Nat Commun 12(1):1–9
Park J, Lühr H, Stolle C, Rodriguez-Zuluaga J, Knudsen DJ, Burchill JK, Kwak Y-S (2016) Statistical survey of nighttime midlatitude magnetic fluctuations: their source location and Poynting flux as derived from the Swarm constellation. J Geophys Res 121:11–235
Park J, Lühr H, Knudsen DJ, Burchill JK (2017) Alfvén waves in the auroral region, their Poynting flux, and reflection coefficient as estimated from Swarm observations. J Geophys Res 122:2345–2360
Press WH, Teukolsky SA, Vetterling WT (1992) Numerical recipes and flannery. Cambridge University Press
Rehman S, Burchill JK, Eriksson A, Marchand R (2012) Earth magnetic field effects on Swarm electric field instrument. Planet Space Sci 73:145–150
Rehman SU, Marchand R, Berthelier JJ, Onishi T, Burchill JK (2013) Earth magnetic field effects on particle sensors on LEO satellites. IEEE Trans Plasma Sci 41:3402–3409
Rodríguez-Zuluaga J, Stolle C, Park J (2017) On the direction of the Poynting flux associated with equatorial plasma depletions as derived from Swarm. Geophys Res Lett 44:5884–5891
Sangalli L, Knudsen D, Larsen M, Zhan T, Pfaff R, Rowland D (2009) Rocket-based measurements of ion velocity, neutral wind, and electric field in the collisional transition region of the auroral ionosphere. J Geophys Res Space Phys 114, A04306
Shen Y, Knudsen DJ, Burchill JK, Howarth AD, Yau AW, Miles DM, James HG, Perry GW, Cogger L (2018) Low-altitude ion heating, downflowing ions, and BBELF waves in the return current region. J Geophys Res Space Phys 123:3087–3110
St-Maurice J-P, Schunk RW (1979) Ion velocity distributions in the high-latitude ionosphere. Rev Geophys Space Phys 17:99
Storey LRO (1998) What's wrong with space plasma metrology? In: Pfaff RF, Borovsky JE, Young D, eds. Measurement techniques in space plasmas: particles, vol 102 of Geophysical monograph series, p 17, American Geophysical Union,
Whalen BA, Knudsen DJ, Yau AW, Pilon AM, Cameron TA, Sebesta JF, McEwan DJ, Koehler JA, Lloyd ND, Pocobelli G, Laframboise JG, Li W, Lundin R, Eliasson L, Watanabe S, Campbell GS (1994) The Freja F3C cold plasma analyzer. Space Sci Rev 70(1):541
Wu J, Knudsen D, Gillies D, Donovan E, Burchill J (2017) Swarm observation of field-aligned currents associated with multiple auroral arc systems. J Geophys Res Space Physics 122:10–145
Wu J, Knudsen D, Gillies DJ, Burchill JK (2020) Swarm survey of Alfvénic fluctuations and their relation to nightside field-aligned current and auroral arc systems. J Geophys Res 125:e2019JA027 220
Zou Y, Nishimura Y, Burchill JK, Knudsen DJ, Lyons LR, Shiokawa K, Buchert SC, Chen S, Nicolls MJ, Ruohoniemi JM et al (2016) Localized field-aligned currents in the polar cap associated with airglow patches. J Geophys Res 121:10–172

Publisher's Note